J. Indian Inst. Sci., July–Aug. 2000, **80**, 363–394.

IISc THESES ABSTRACTS

Thesis Abstract M.Sc.(Engng)

Optimal regular tree pattern matching using pushdown automata by Maya Madhavan
Research supervisor: Prof. Priti Shankar
Department: Computer Science and Automation

1. Introduction

Linear regular tree pattern matching is a problem that has direct application to the generation of tools for rear ends of compilers. The problem can be stated as follows: Given a regular tree grammar, construct an automaton which recognizes trees generated by the grammar. Conventional approaches to this problem[1–7] generate finite-state tree automata. We cast the problem as a parsing problem for context-free languages generated by grammars that are in general highly ambiguous, though restricted in form. This restriction enables us to generate linear time recognizers that are actually deterministic pushdown automata.

Usually, for the problem of code generation, each production represents a machine instruction and is augmented with an instruction cost. These costs are used during matching in selecting an optimal sequence of patterns that match a subject tree. Cost analysis may be performed either statically, that is, at pattern processing time, or dynamically, that is, at code generation time.

Some grammars permit static cost precomputation with costs incorporated into the states of a finite-state tree pattern matching automaton.[3, 6–8] We show that for some grammars it is possible to incorporate costs into the states of the deterministic pushdown automaton (DPDA) so that cost analysis can be performed at pattern preprocessing time. There are input instances for which, the DPDA is much smaller in size than the finite tree automaton generated. Also, for optimal matching, our approach handles a larger class of grammars than that handled by previous approaches.

The results of this work can be applied to the problem of instruction selection for code generation. Previous techniques used are LR parsing,[9] tree rewriting[6, 8] and tree pattern matching.[2–5, 7, 10]

Tree pattern matching has several other applications also, such as automatic theorem proving, implementation of functional languages, term rewriting systems, etc.

2. Tree pattern matching

The two basic approaches to tree pattern matching are the top down and the bottom up methods based on the direction of traversal of the subject tree. Top down tree pattern matching reduces tree matching to string matching.[1, 4, 11] It uses the string matching algorithm of Aho and

Corasick.[12] For the given set of patterns, trees are constructed and used to form the matching automaton. The algorithm to construct the matching automaton takes time linear in the size of the pattern forest. The matching time is nonlinear and depends on the patterns and the subject tree. Top-down approach has been used for code generation in Tjiang.[13]

Bottom-up tree matching generalizes string matching. The basic idea[1] is to find the set of all matching patterns and subpatterns at all the nodes of the given subject tree. The set of matching patterns at a node is called the *matchset* at that node. Given the matchset at all the q children of a q-ary operator at node n, we can find the set of matching patterns at n. Since the patterns are finite, we can precompute all the possible matchsets, encode them and enter the information into tables. There are separate tables for each operator and a q-ary operator has a q-dimensional table. The q indices are the codes for the matchsets at the q children and the entry in the table is the code for the matchset at the node under consideration. The table size is therefore exponential in the maximum arity of the operators. The tables are also rather sparse. Chase[2] suggested that these tables could be compressed using equivalence relations between matchsets, yielding substantial reduction in sizes. The technique of Chase has been used for input specifications corresponding to regular tree grammars.[3]

Regular tree grammars can be augmented by associating a cost with each rule in P. Differential costs can be included into the states of the matching automaton to avoid cost computations at matching time.[3, 7] This avoids expensive cost analysis at code generation time.

3. New algorithm for regular tree pattern matching

Given a regular tree grammar, one can construct a DPDA as recognizer. In Gantait[10] an algorithm for constructing a DPDA is given, which begins with the LR(0) automaton for the grammar, and then modifies it by merging states. A code generator which performs optimal matching at code generation time has been automatically generated for the MC68000 series. Cost analysis is performed dynamically, i.e. at code generation time.

We present new algorithms for both regular tree pattern matching, and optimal regular tree pattern matching where a minimum cost sequence of tree replacements is obtained. The first algorithm is based on the Earley parsing algorithm for context-free languages.[14] The tree parsing problem is to find the set of all derivation trees in the regular tree grammar for a subject tree starting from some specified nonterminal. Our goal is to generate a tree parser generator that takes as input a regular tree grammar and returns as output a tree parser for the grammar. The matching problem is to find all possible tree derivations for a subject tree given the regular tree grammar. Consider a new context-free grammar obtained by replacing the right-hand sides of the productions of the regular tree grammar by the post-order listings of the corresponding trees. Since operator arities are fixed, there is a unique correspondence between trees and their post-order listings. Finding all tree derivations in the regular tree grammar corresponds to finding all string derivations in the context-free languages. The bottom-up DPDA we construct reports a match of pattern p at node n of the subject tree whenever it reduces by production for pattern p after consuming the symbol at node n (in post-fix order). In general, reductions by more than one production are possible at a node and the parser carries the effect of multiple reductions.

The tables that are generated are two dimensional irrespective of the arity of the operators. There are two tables, δ_A and δ_{LC}, that encode the DPDA. The combined size of the tables is $O((|A| + 2^{|NT|})2^{patsize})$ where $|A|$ is the alphabet size, $|NT|$ the number of nonterminals and *patsize* the total size of all tree patterns or equivalently, the sum of the lengths of all the right-hand sides of production. The technique of Chase[2], when applied to regular tree grammars, requires space $O(|OP|(2^{|NT| \times maxarity} + maxarity \times 2^{patsize}))$ where $|OP|$ is the total number of operators of the grammar, and *maxarity* is the maximum arity of an operator.

4. Optimal tree pattern matching

Using the algorithm just described, one option is to perform cost computations at code generation time using dynamic programming, as in Gantait.[10] Another option is to perform cost computations at preprocessing time and include the information in the states of the automaton.

We extend the technique of Balachandran *et al.*[3] and present a strategy for building a DPDA augmented with costs, thus performing cost computations at preprocessing time. This DPDA will generate optimal code without the need to perform cost analysis at matching time. However, not all regular tree grammars are amenable to this technique. In some cases, the input may be such that the cost does not converge at any height. Thus there is no finite automaton with precomputed costs for such grammars. In such cases, the only solution is to perform runtime cost computations. We have derived a sufficient condition for convergence. The inclusion of cost into the automaton increases the number of states of the automaton and in certain cases, the blow up in the number of states renders it impractical.

5. Implementation

The preprocessor and the matcher generator have been implemented. The preprocessor has three parts: pattern input, precomputation and table construction. In the pattern input phase, written using Yacc, the input regular tree grammar is input from the user and converted into suitable internal representation. The precomputation phase computes certain structures that make the table construction easier. In the table construction phase, the tables representing the DPDA are constructed.

The matcher–generator takes the tables and creates the C-programs that perform matching. The automatically generated set of programs include a Lex function to read the user input, functions to recreate the productions of the grammar and the matchsets in memory and create the tree for the given input, the main matching function which traverses the tree bottom up, the function to traverse the tree top down and select the minimum cost derivation and finally the function to traverse the tree bottom up and display the selected productions.

6. Results and conclusion

The new algorithm works well in most cases, enabling cost information to be included into the matching automaton. However, the patterns for the MC68000 generates more than 35,000 states when compared with 482 states when costs are not precomputed. For such examples, cost computation by dynamic programming is recommended. The patterns for the IBM R6000 yields 112 states with costs. For the Intel Pentium, the algorithm yields 565 states with costs.

The tree pattern matcher can be easily extended to generate code. The pattern input function has to be augmented to read directives to the code generator and also actions for the patterns. The bottom-up pass of the matcher has to be extended to emit code depending upon the selected pattern. Instruction scheduling and register allocation phases have to be added to generate efficient code.

References

1. HOFFMAN, C. AND O'DONNELL, M. J. — Pattern matching in trees, *J. ACM*, 1982, **29**, 68–95.
2. CHASE, D. R. — An improvement to bottom-up tree pattern matching, *Proc. 14th ACM Symp. on Principles of Programming Languages*, 1987, pp. 168–177.
3. BALACHANDRAN, A., DHAMDHERE, D. M. AND BISWAS, S. — Efficient retargettable code generation using bottom-up tree pattern matching, *Computer Languages*, 1990, **15**, 126–140.
4. AHO, A. V. AND GANAPATHI, M. — Efficient tree pattern matching: An aid to code generation, *Proc. 12th Annual Symp. on Principles of Programming Languages*, Jan. 1985, pp. 334–340.
5. HATCHER, P. J. AND CHRISTOPHER, T. W. — High quality generation via bottom-up tree pattern matching, *Proc. 13th ACM Symp. on Principles of Programming Languages*, 1986, pp. 119–129.
6. PELEGRI-LLOPART, E. — *Rewrite systems, pattern matching, and code generation*, Ph.D. Thesis, Technical Report UCB/CSD 88/423, Computer Science Division, University of California, Berkeley, 1988.
7. FERDINAND, C., SEIDL, H. AND WILHELM, R. — Tree automata for code selection, *Acta Inf.*, 1994, **31**, 741–760.
8. PELEGRI-LLOPART, E. AND GRAHAM, S. L. — Optimal code generation for expression trees: An application of BURS theory, *Proc. 15th ACM Symp. on Principles of Programming Languages*, 1986, pp. 119–129.
9. GLANVILLE, R. S. AND GRAHAM, S. L. — A new method for compiler code generation, *Proc. 5th ACM Symp. on Principles of Programming Languages*, Jan. 1978, pp. 231–240.
10. GANTAIT, A. — *Design of a bottom-up tree pattern matching algorithm and its application to code generation*, M. E. Project Report, Department of Computer Science and Automation, Indian Institute of Science, Bangalore, India, 1996.
11. AHO, A. V., GANAPATHI, M. AND TJIANG, S. W. K. — Code generation using tree matching and dynamic programming, *ACM TOPLAS*, 1989, **11**, 491–516.
12. AHO, A. V. AND CORASICK, M. J. — Efficient string matching: An aid to bibliographic search: *Commun. ACM*, 1975, **18**, 333–340.
13. TJIANG, S. W. K. — *Twig reference manual*, CSTR-120, AT&T Bell Laboratories, Murray Hill, New Jersey, 1985.
14. EARLEY, J. — An efficient context-free parsing algorithm, *Commun. ACM*, 1970, **13**, 94–102.

Thesis Abstract (M.Sc.(Engng))

Numerical flow–acoustic simulation of engine exhaust systems by Y. Sathyanarayana
Research supervisor: Prof. M. L. Munjal
Department: Mechanical Engineering

1. Introduction

Predicting radiated noise requires a model of the acoustic behavior of the intake/exhaust system and a model of the engine cycle source characteristics. This is often dealt with either in the frequency- or in the time-domain analysis. The frequency-domain analysis of mufflers is done by means of transfer matrix method. This is quite convenient and all commercial automotive mufflers are analyzed in this domain.[1] But it is basically a linear analysis and needs a prior knowledge of the aeroacoustic source characteristics, the evaluation of which remains a challenge. The time-domain analysis of the exhaust systems, on the other hand, is a fully nonlinear analysis and is usually done using the method of characteristics.[2] It offers a completely independent formalism for muffler analysis in as much as it obviates the necessity of a prior knowledge of the aeroacoustic source characteristics. But this analysis has been primarily developed and used for thermodynamic performance evaluation and not for the aeroacoustic performance evaluation of the exhaust system. It is very time consuming. Moreover, this is limited to a few simple muffler elements only. The hybrid approaches developed recently attempt at combining the frequency-domain approach with the finite wave time-domain approach with a view to incorporate advantages of both.[3–5] However, they tend to be rather cumbersome because of the repeated use of the Fourier transform pair, and do not reproduce adequately the peaks and troughs observed experimentally in the frequency spectra of the radiated sound pressure level.

The investigation leading to the present work is limited to filling up some of the lacunae that have been pointed out in the preceding paragraph. The extended-tube expansion chamber is analyzed by means of the two as well as three characteristics approach. The simulated results obtained by the two approaches are compared. It is observed that the two characteristics approach is a very good approximation to the three characteristics approach, and would therefore be adequate for modeling complex muffler elements. In the hybrid approach, cylinder/cavity is analyzed in the time domain to calculate the exhaust mass flux history at the exhaust valve by means of the method of characteristics, avoiding the tedious meshing and interpolation procedure. Various results of this approach are validated by means of the method of characteristics and the linear acoustic theory, and various peaks and troughs in insertion loss curves are analytically validated.

2. Finite wave modeling of the extended-tube resonator

In the three characteristics approach (MOC-3), there are two known and seven unknown variables across an extended-tube resonator junction. Mass continuity, energy, momentum and entropy equations along with compatibility equations are simultaneously solved by means of the Newton–Raphson method to evaluate the unknown variables. Interpolation technique explained in Gupta and Munjal[6] is implemented here to calculate the characteristics variables at

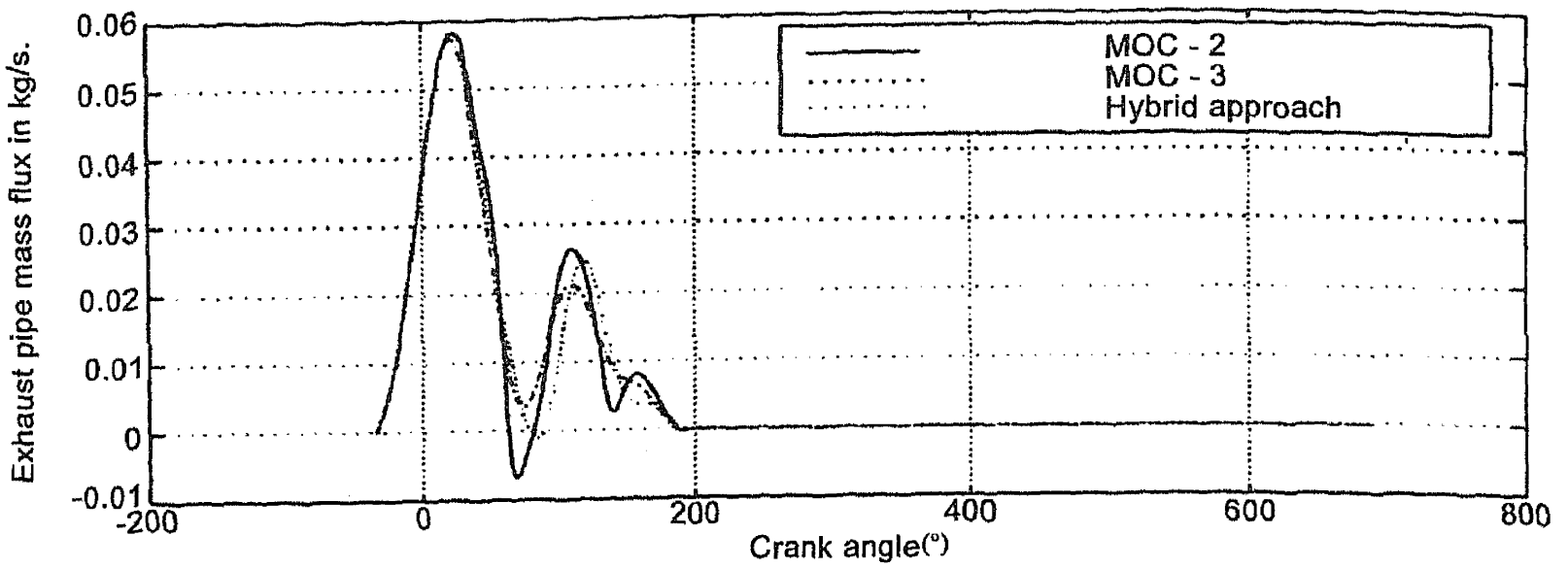

FIG. 1. Exhaust mass flux history of an extended-tube expansion chamber muffler.

all the instants. Following Gupta's experimental observations, the blowdown pressure and temperature were taken as 0.3436 MPa and 1300 K, respectively.[7] Typical steady-state results of such a simulation for the extended-tube expansion chamber are shown in Figs 1 and 2.

From the results presented in Figs 1 and 2, it is evident that in case of mufflers such as extended-tube expansion chamber, the two characteristics approach (MOC-2) is in good agreement with the full nonlinear three characteristics solution. Differences in the two approaches are more pronounced at higher frequencies only which are not so very important for designers.

3. Hybrid approach for aeroacoustic analysis of the engine exhaust systems

Acoustic pressure and volume velocity may be written in terms of the progressive wave variables A and B, where A represents the forward wave and B the reflected wave.[1] The corresponding time-domain variables are denoted by P and Q, respectively, in this work. We can interrelate these variables as follows:

$$P = 1 + \frac{\gamma - 1}{\gamma} \frac{A}{p_0} \tag{1}$$

and

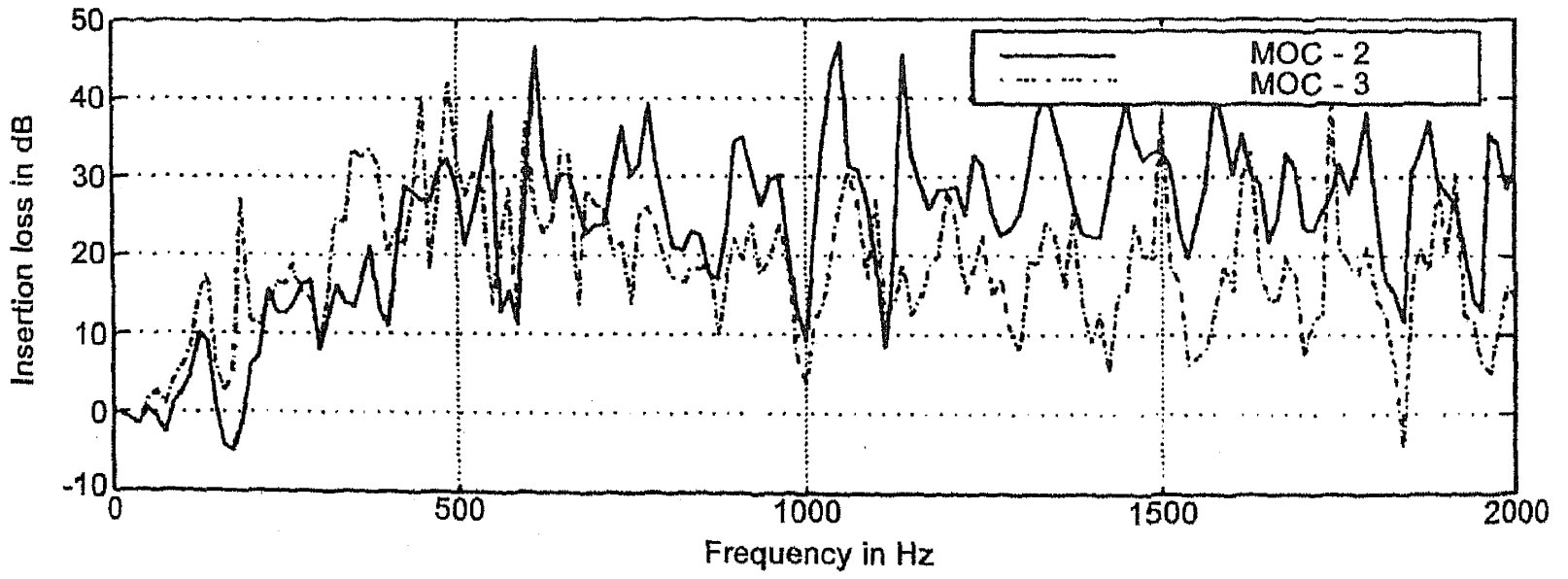

FIG. 2. Insertion loss of an extended-tube expansion chamber muffler.

$$Q = 1 + \frac{\gamma - 1}{\gamma} \frac{B}{p_0}. \tag{2}$$

Neglecting the effects of nonlinear propagation in the exhaust pipe and assuming free expansion at the radiation end of the exhaust pipe, as the effect of radiation condition/impedance would be negligible, the fluctuating pressure would be given by

$$A(t - \tau) + B(t) = 0 \tag{3}$$

at the valve end, where τ is the time taken by the forward progressive wave to traverse the exhaust pipe up and down. It can symbolically be written as

$$\tau = 2 \frac{l_{ex}}{a_0}. \tag{4}$$

Substituting eqns (1) and (2) in eqn (3) gives

$$Q(t) = 2 - P(t - \tau). \tag{5}$$

This means that Q at the present instant of time can be evaluated by using the P wave that started τ seconds ago. This way, meshing and interpolation in the pipe can be avoided and all the attention will be limited to the valve end only.

During the initial phase of the first cycle of calculations, we can take

$$Q(t) = 1 \text{ for } t \leq \tau. \tag{6}$$

In the case of a muffler proper, expansion from the exhaust pipe into the first chamber can be assumed to be free expansion. Thus, eqns (4)–(6) may still be applicable with a new value of l_{ex} and hence the time lag τ. The same analysis can be used on the intake side also.

At all instants of time, the mass flux $\dot{m}(t)$ from the valve end is calculated using values of the characteristic variables P and Q. Taking Fourier transform of $\dot{m}(t)$, $v_{c,n}(\omega)$ is obtained. This may be combined with the linear frequency domain model of the exhaust system to calculate $v_{c,0}(\omega)$. The convective mass velocity $v_{c,0}$ is then used to calculate the power radiated from the tail pipe end.[1] The procedure is repeated with and without the given muffler to calculate insertion loss of the muffler.

Exhaust mass flux history for extended-tube expansion chamber is plotted in Fig. 1. The thermodynamic analysis of an engine with the hybrid approach is quite satisfactory when compared with the method of characteristics. Tedious procedure of meshing, interpolation and solving a number of equations simultaneously are avoided in this approach, which saves much time and effort.

Insertion loss values of the extended-tube resonator muffler are shown in Fig. 3. The results of the hybrid approach are compared with those of the pure acoustic theory, where the source is approximated as a constant velocity source (infinite source impedance). Prediction of the hybrid approach and pure acoustic theory are seen to be close to each other.

Thus, results of the hybrid approach tally quite well with those of the time-domain and frequency-domain approaches.

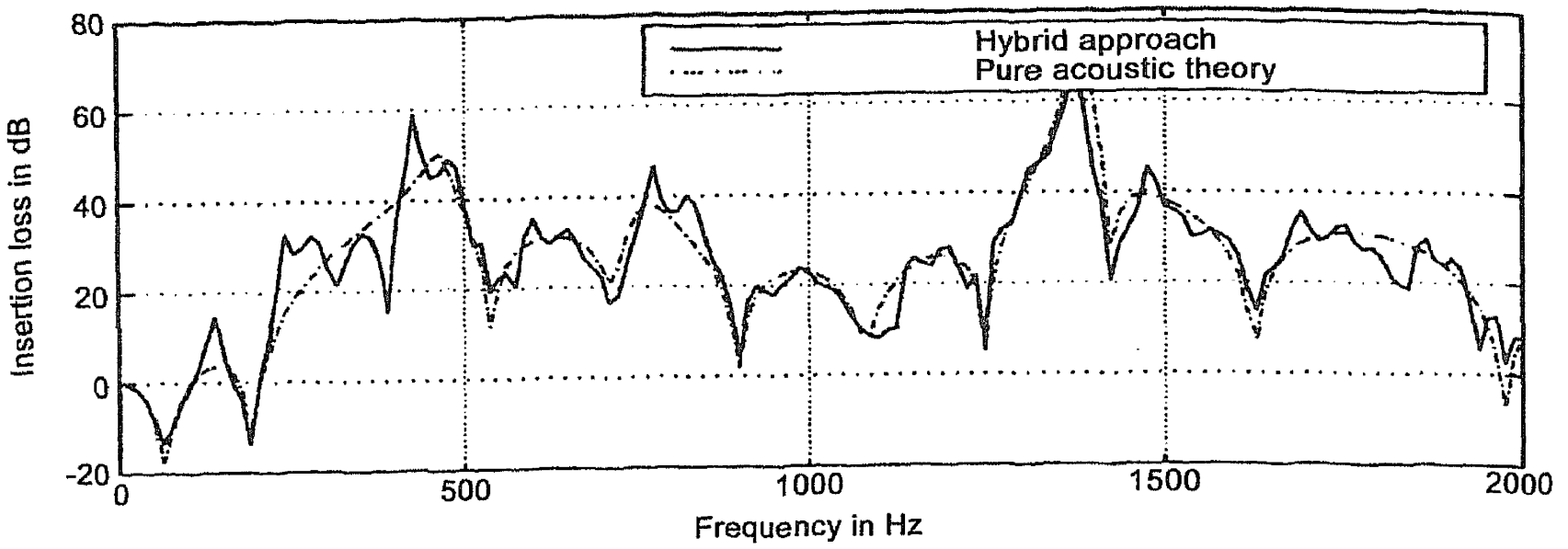

FIG. 3. Insertion loss of an extended-tube expansion chamber muffler.

References

1. MUNJAL, M. L. — *Acoustics of ducts and mufflers*, Wiley Interscience, 1987.
2. BENSON, R. S. — *The thermodynamics and gas dynamics of internal combustion engines*, Clarendon Press, 1982.
3. JONES, A. D., MOORHEM, W. K. V. AND VOLAND, R. T. — Is a full nonlinear method necessary for the prediction of radiated engine exhaust noise? *Noise Control Engng J.*, 1986, **26**(2), 74–80.
4. DAVIES, P. O. A. L. — Aeroacoustics and time varying systems, *J. Sound Vibration*, 1996, **190**, 345–362.
5. PAYRI, F., DESANTES, J. M. AND TORREGROSA, A. J. — Acoustic boundary conditions for unsteady one-dimensional flow calculations, *J. Sound Vibration*, 1995, **188**, 85–110.
6. GUPTA, V. H. AND MUNJAL, M. L. — Time-domain-finite-wave analysis of the engine exhaust system by means of the stationary-frame method of characteristics. Part I. Theory, *Sādhanā*, 1993, **18**, 911–925.
7. GUPTA, V. H. AND MUNJAL, M. L. — Time-domain-finite-wave analysis of the engine exhaust system by means of the stationary-frame method of characteristics. Part II. Computed results and experimental corroboration thereof, *Sādhanā*, 1993, **18**, 927–941.

Thesis Abstract (Ph.D.)

Growth and characterization of Indium antimonide and its heterostructures by R. Venkataraghavan
Research supervisors: Prof. H. L. Bhat and Dr. K. S. R. Koteswara Rao
Department: Physics

1. Introduction

Since the discovery of the III–V semiconductors by Welker,[1] indium antimonide has become one of the prominent materials in the forefront of research. On account of its high mobility, narrow bandgap and ease of preparation, this material has been extensively used in IR detectors and high-speed devices. A variety of techniques have been applied to grow it, though the efficacy of these methods varies widely.[2–7] This work is concerned with the growth and other

aspects of InSb both in the bulk and in thin-film form. It also presents the work on a-Si:H/InSb-switching devices.[8]

2. Bulk crystal growth

Various methods have been employed to grow InSb, in the past which include vertical and horizontal Bridgman. In spite of considerable success, the growth of large homogeneous single crystals still remains a problem. Recent studies during vertical Bridgman growth have revealed a deviation of the melt–solid interface away from the congruent melting point isotherm (Fig. 1). Experiments show that the position of the melt–solid interface does not match with the congruent melting point isotherm in the vertical Bridgman growth of InSb, which greatly affects the yield and quality of the crystals grown.[2, 3] Further, it is seen that changing the temperature gradient across the melt–solid interface and imposing optimum values to lower the rate of the ampoule could help in stabilizing the interface at the congruent melting-point iso-

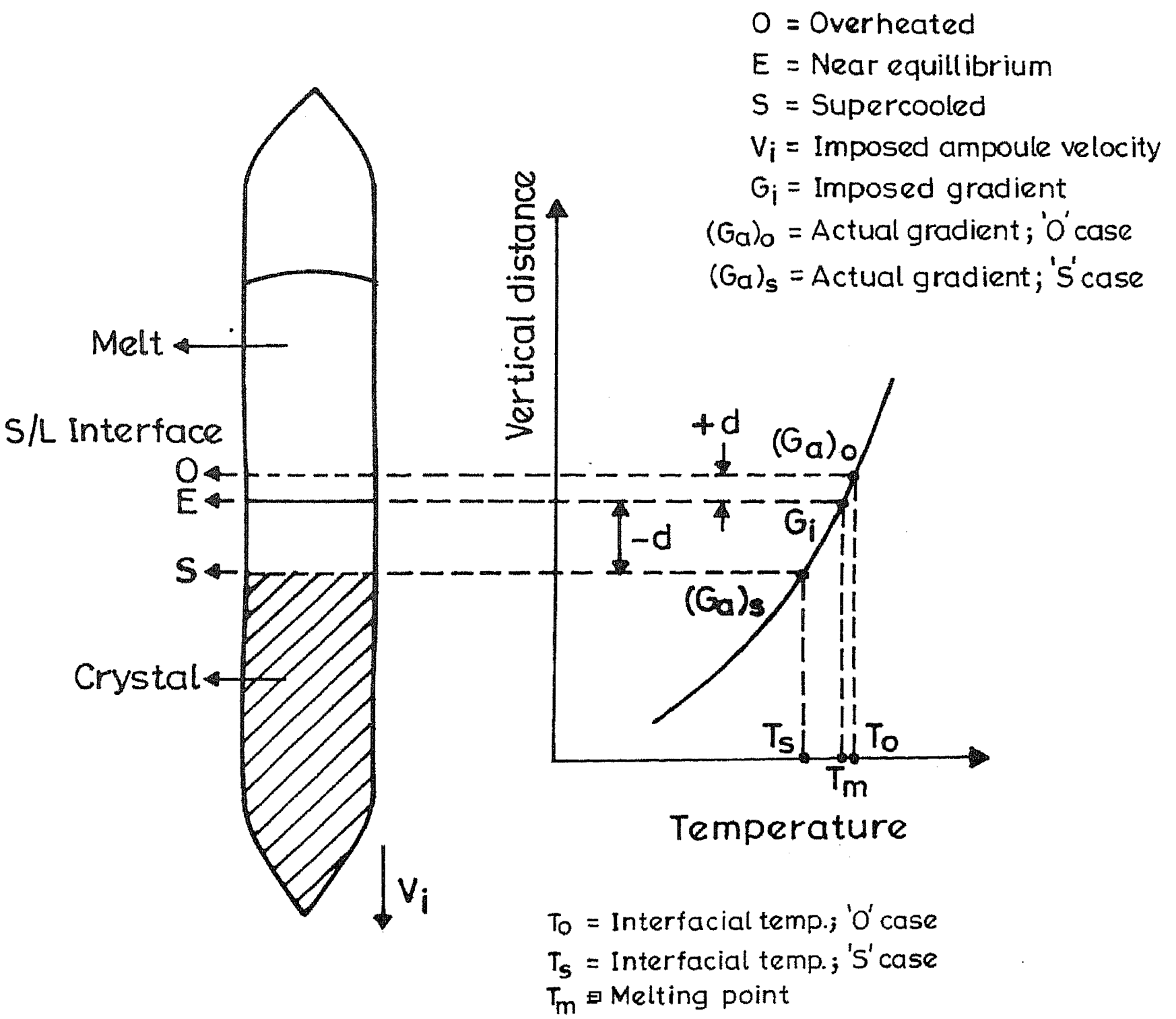

FIG. 1. Schematic of the ampoule in vertical Bridgman growth showing the melt–solid interface during growth.

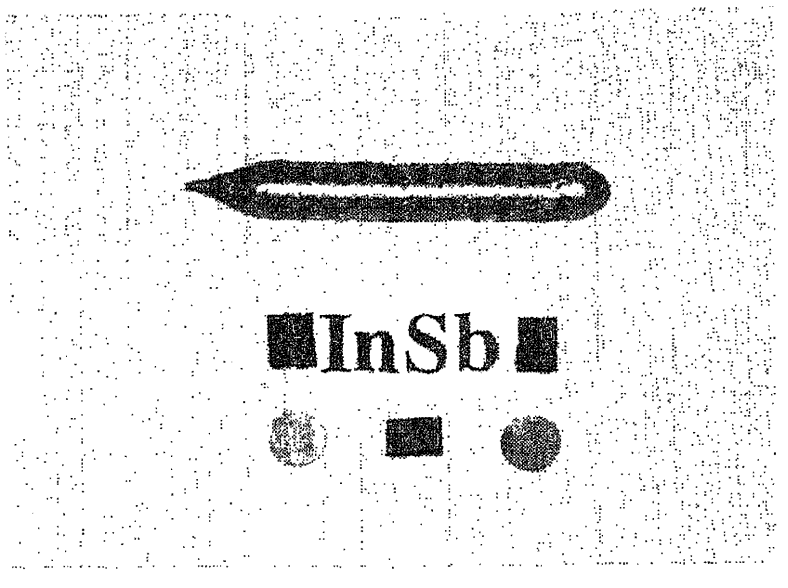

FIG. 2. Single-crystal InSb boules grown by the vertical Bridgman technique.

therm. Crystals were grown under a variety of conditions by varying temperature gradients and lowering velocities. Three conditions of growth, viz. overheated, supercooled and near-equilibrium, could be identified with the changing gradients and velocities. The crystals grown under the near-equilibrium conditions showed very good grain selection, lower dislocation content as well as very good transport characteristics. Figure 2 shows the InSb boule grown by the vertical Bridgman technique.

InSb bulk single crystals were also grown by the horizontal Bridgman technique in a system built for this purpose. Defect density in the horizontally grown crystals evaluated through etching revealed a pit count of $10^6/cm^2$ as against etch pit density (EPD) of $10^4/cm^2$ in the vertically grown crystals. InSb crystals grown by vertical or horizontal method showed transport properties ranging between an excess carrier concentration of 10^{14} to $10^{15}/cm^3$ and a mobility of 10^5 cm^2/Vs.

3. Thin-film growth

Indium antimonide thin films were grown on InSb and GaAs substrates by liquid phase epitaxy (LPE).[4] While homoepitaxial thin films were grown by the step-cooled technique, ramp-cooling was used to grow InSb/GaAs. An additional sacrificial substrate was used during homoepitaxy to get films with better surface coverage and good morphology (Fig. 3).

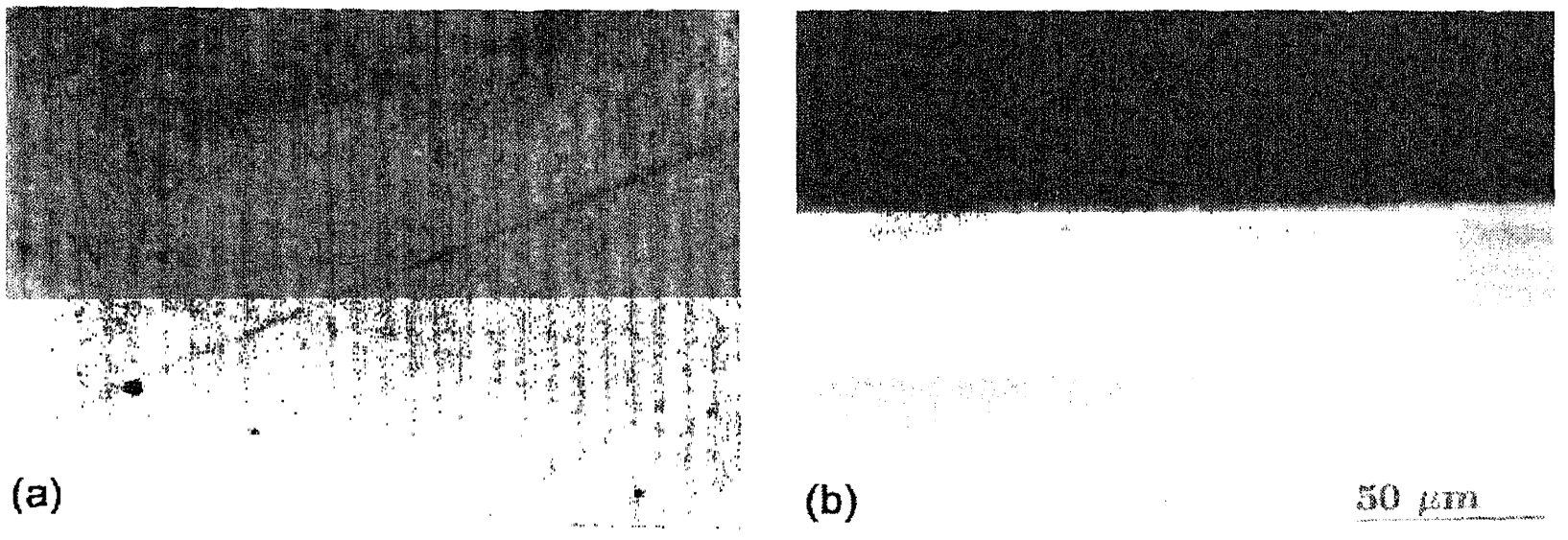

FIG. 3. Photographs of epilayer and interface of InSb/GaAs structure grown by LPE technique.

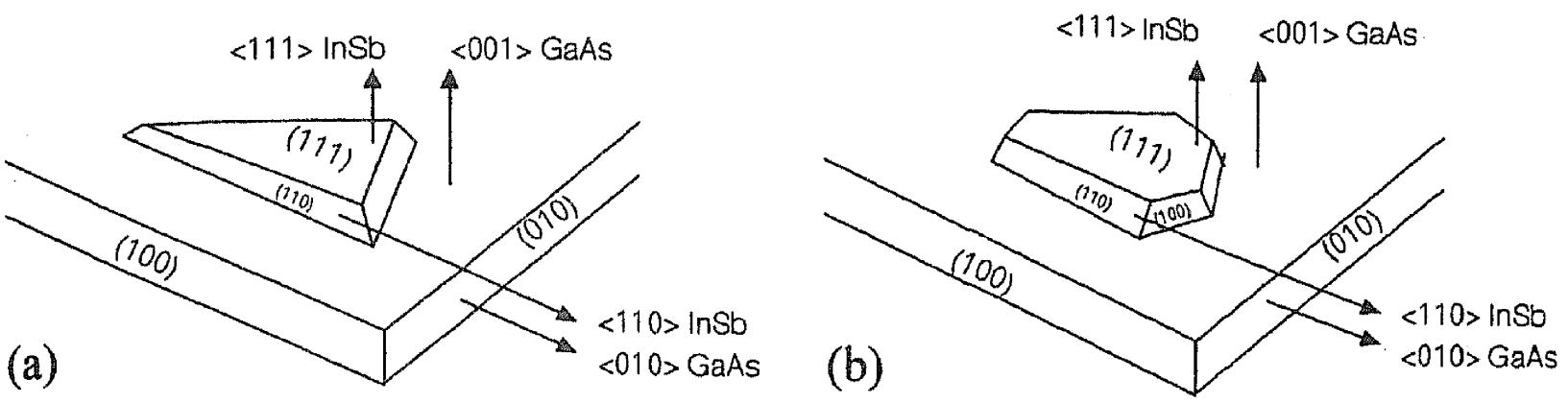

FIG. 4. Schematic of the morphology of InSb nuclei on GaAs substrate.

In the growth of indium antimonide on gallium arsenide, it is seen that the morphology of the nucleating island shows well-defined facets depending on the growth conditions. The nuclei either showed triangular or polygonal morphology (Fig. 4) depending on the imposed supersaturation. InTlSb, a ternary of In, Tl and Sb, extends the range of usefulness of InSb-based detectors to the long wavelength infrared region (LWIR) which makes such structures all the more promising. LPE has been used to grow InTlSb/GaAs and the ensuing heterostructure shows a shift in the absorption band to longer wavelengths ($\cong 10\ \mu m$).

Thin films of InSb have been grown on CdTe substrates by pulsed laser deposition technique. The film quality and stoichiometry have been studied for two laser fluences and various growth parameters. In films grown at higher laser fluence (280 mJ/pulse), pitted morphology was observed but the problem could be alleviated by reducing the laser fluence. Extensive studies were made on the interface of InSb/CdTe heterojunction and the presence of an intermetallic indium telluride was identified. Photoluminescence spectroscopy has been used to infer the presence of In_2Te_3 as against InTe. Further, thermoenergetic calculations at the interface have been used to ascertain the same. The studies on the interface have led to further improvement in growth to yield films of optimum quality.[5, 6]

4. Device structure

Amorphous silicon layers were deposited by glow discharge plasma method on InSb substrates. Ohmic magnesium contacts were evaporated on the surface to make metal/a-Si:H/InSb devices. I–V characteristics of the device showed properties similar to InSb surface barrier diodes. However, at reverse bias, the device switches from a low to a high resistance state (Fig. 5). The threshold switching is seen to shift with temperature and resembles ovonic switching. A simple band model has been used to explain the observed effects in a-Si:H/InSb.[7]

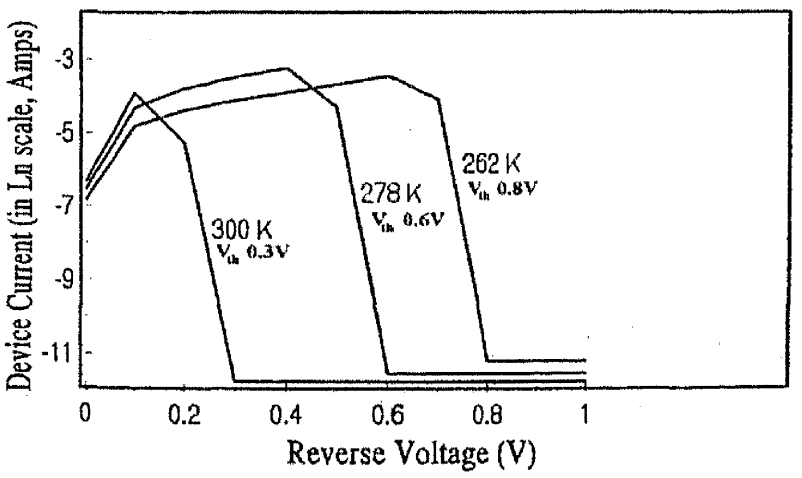

FIG. 5. I-V characteristic of a-Si:H/InSb heterostructure showing switching.

5. Conclusion

Indium antimonide has been grown by a variety of techniques. These include bulk techniques like vertical and horizontal Bridgman techniques and thin-film methods like LPE and PLD. Devices made from a-Si:H/InSb show interesting low-threshold switching.

References

1. WELKER, H. *Z. Naturf. A*, 1992, **7**, 744.
2. VENKATARAGHAVAN, R., RAO, K. S. R. K. AND BHAT, H. L. *J. Phys. D: Appl. Phys.*, 1997, **30**, L61.
3. VENKATARAGHAVAN, R., RAO, K. S. R. K. AND BHAT, H. L. *J. Cryst. Growth*, 1998, **186**, 322.
4. VENKATARAGHAVAN, R. *et al.* *Bull. Mater. Sci.*, 1998, **22**, 133–137.
5. VENKATARAGHAVAN, R. *et al.* *Bull. Mater. Sci.*, 1996, **19**, 123.
6. VENKATARAGHAVAN, R., RAO, K. S. R. K., HEGDE, M. S. AND BHAT, H. L. *Physica Status Solidi (a)*, 1997, **163**, 93.
7. VENKATARAGHAVAN, R., RAO, K. S. R. K., BHAT, H. L., PAL, S. AND DUBEY, G. C. *Solid St. Commun.*, 1997, **102**, 759.

Thesis Abstract (Ph. D.)

Electrical and thermal studies on metal doped germanium telluride glasses by K. Ramesh
Research supervisors: Prof. E. S. Rajagopal and Dr. K. S. Sangunni
Department: Physics

1. Introduction

Binary Ge-Te chalcogenide glasses exhibit interesting structural phase transitions like sharp discontinuous semiconductor-to-metal transition, double T_g and double T_c under high pressures and temperatures.[1] The stability, rigidity and structural connectivity of chalcogenide glasses are found to change in a special way when metal atoms are added.[2] For example, the addition of Ag to selenide glasses introduces ionic bonding and the conduction changes from electronic to ionic conduction. In contrast, Ag with germanium tellurides results only in covalent bonding and the conduction is purely electronic.[3]

This work deals with thermal and electrical resistivity studies of Ag- and Cu-doped Ge-Te glasses as function of composition at high pressures and temperatures. The aim of this work is to study the network connectivity of Ge-Te glasses and the pressure-induced semiconductor-to-metal transition when the glasses are doped with Cu and Ag atoms.

2. Experimental

Bulk $Cu_xGe_{15}Te_{85-x}$ ($2 \leq x \leq 10$) and $Ag_xGe_{15}Te_{85-x}$ ($2 \leq x \leq 21.5$) glasses are prepared by melt-quenching method. The amorphous nature of the prepared samples is confirmed by X-ray diffraction (XRD).

Differential scanning calorimetric (DSC) studies on Cu-Ge-Te and Ag-Ge-Te glasses are conducted to evaluate the thermal parameters T_g, T_c and T_m. The heating rate dependence of these parameters is also measured to estimate the activation energy for crystallization (E_c). Electrical resistivity measurements at high pressures and temperatures (450–77 K) have been undertaken in a Bridgman anvil apparatus. To generate high-temperature studies a heater around the anvil is used.

3. Results and discussion

3.1. *DSC studies on Cu-Ge-Te and Ag-Ge-Te glasses*

Both $Cu_xGe_{15}Te_{85-x}$ and $Ag_xGe_{15}Te_{85-x}$ glasses show a single glass transition T_g followed by a single crystallization T_c upon heating whereas binary Ge-Te glasses exhibit a double T_g and double T_c. The composition dependence of T_g of $Cu_xGe_{15}Te_{85-x}$ samples exhibits a minimum at $x = 5$, whereas the T_c and E_c show maximum at $x = 5$. X-ray studies on the samples annealed at their respective crystallization temperatures yield only hexagonal Te and rhombohedral -Ge-Te phases. This indicates that Cu atoms do not form their own structural units with Ge or Te. It is likely that Cu atoms randomly replace Ge as their atomic radii, electronegativity and coordination are similar.[4]

The variation of the thermal parameters T_g, T_c, E_c and thermal stability ($\square T$) with composition for $Ag_xGe_{15}Te_{85-x}$ glasses show a minimum at $x = 5$. T_g shows a maximum at $x = 18.5$, whereas T_g, T_c, E_c and $\square T$ exhibit a minimum at $x = 18.5$. The X-ray patterns of the devitrified samples can be indexed to cubic Ag_8GeTe_6, cubic $GeTe_4$ and hexagonal Te phases. According to the present results the network structure of these glasses can be viewed as having three structural regions consisting of Te chains, Ag-Te and Ge-Te tetrahedral units. For $x \leq 5$, flexible Te chains are more active resulting in a minimum in T_g at $x = 5$. In the second region ($7.5 \leq x \leq 15$) Ag-Te and Ge-Te tetrahedral units influence the structure more and the structural rigidity grows as these units are rigid causing an increase in T_g, T_c and E_c. At $x = 15$, Ge-Te and Ag-Te units are equally populous; so a crossover from Ge-Te to Ag-Te results in a plateau region around $x = 15$.

The thermal crystallization studies provide a clue to understand the different ranges of glass formation in $Cu_xGe_{15}Te_{85-x}$ ($0 \leq x \leq 10$) $Ag_xGe_{15}Te_{85-x}$ ($0 \leq x \leq 23$). To improve the glass-forming ability the added third element should increase the network connectivity by interacting with the existing parent glass matrix. The added Cu atoms do not improve the network connectivity of the parent Ge-Te glass matrix as evident from the X-ray studies. The addition of Ag to Ge-Te glasses promotes the network connectivity resulting in a wide range of glass formation.[4]

It has been suggested that the network of covalent network glasses undergoes a transition form floppy to a rigid structure in a percolative manner (rigidity percolation). This change occurs at a critical composition corresponding to the average coordination number $Z_{av} = 2.40$. Unusual changes in the properties of covalent network glasses are expected at this critical composition.[5] The unusual change in T_g, T_c, E_c and $\square T$ at $x = 5$ is the indication of the rigidity percolation in these glasses. In addition to the rigidity percolation, a chemical ordering also

occurs at a higher average coordination number. The unusual change at $x = 18.5$, in $Ag_xGe_{15}Te_{85-x}$ glasses is due to chemical ordering in the structural network.[5]

3.2. *High-pressure studies on Cu-Ge-Te and Ag-Ge-Te glasses*

Electrical resistivity measurements at high pressures and low temperatures indicate that both $Cu_xGe_{15}Te_{85-x}$ and $Ag_xGe_{15}Te_{85-x}$ glasses undergo a continuous semiconductor–metal transition around 4–5 GPa pressure. The activation energy for electrical conduction ($\square E$) calculated from $\log(\rho/\rho_o)$ vs $1/T$ plots decreases with pressure. $\square E$ decreases due to the reduction of the band gap at high pressures. In the $Cu_xGe_{15}Te_{85-x}$ glasses, a maximum in $\square E$ and the resistivity at ambient conditions is observed at $x = 5$.[4] The conductivity activation energy of $Ag_xGe_{15}Te_{85-x}$ shows a minimum at $x = 5$ and a turn around $x = 18.5$. The anomaly seen at $x = 5$ corresponds to the rigidity percolation and that seen at $x = 18.5$ corresponds to the chemical ordering threshold.[4]

The resistivity as a function of temperature (300–450 K) of $Cu_5Ge_{15}Te_{80}$ glass at various pressures shows a subtle change around the glass transition temperature. T_g measured from the $\log(\rho/\rho_o)$ vs $1/T$ is found to decrease with an increase in pressure. The model developed by deNeufville and Rockstad finds a linear relationship between glass transition temperature and optical band gap (E_g). This model can be used to explain the observed behaviour. In chalcogenide glasses, $\square E$ and E_g are related by $\square E \approx E_g/2$. Decrease in $\square E$ at high pressures indicates a reduction in E_g. The decrease in E_g shifts the T_g of $Cu_5Ge_{15}Te_{80}$ to lower values.

Under high electric field $Cu_xGe_{15}Te_{85-x}$ and $Ag_xGe_{15}Te_{85-x}$ glasses are found to exhibit memory switching. The memory switching and the composition dependence of switching fields are explained on the basis of thermally induced phase transitions in these glasses at high fields. The switching fields of both the glasses decrease with the composition and exhibit anomalies at compositions corresponding to rigidity percolation and chemical ordering thresholds.

The present studies show that the thermal, electrical and structural properties of chalcogenide glasses as well as the anomalies expected at the topological and chemical thresholds are to a large extent determined by the atomic size, relative covalency and coordination of the added impurities.

References

1. ASOKAN, S., PARTHASARATHY, G. AND GOPAL, E. S. R. — *Phil. Mag. B*, 1988, **57**, 49.
2. BORISOVA, Z. U. — *Glassy semiconductors*, Plenum Press, 1985, p. 436.
3. FERHAT, A., OLLITRAULT-FICHET, R., MASTELARO, V., BENAZETH, S. AND RIVET, R. J. — *J. Phys. IV*, 1992, **C2**, 201.
4. RAMESH, K., ASOKAN, S., SANGUNNI, K. S. AND GOPAL, E. S. R. — *J. Phys.: Condensed Matter*, 1996, **8**, 2755; *Phys. Chem. Glasses*, 1996, **37**, 17.
5. PHILLIPS, J. C. AND THORPE, M. F. — *Solid St. Commun.*, 1985, **53**, 699.

Thesis Abstract (Ph.D.)

Molecular characterization of hemagglutinin (H) surface glycoprotein of Peste des petits ruminants virus (PPRV) by Shyam Gajavelli
Research supervisor: Prof. M. S. Shaila
Department: Microbiology and Cell Biology

1. Introduction

Peste des petits ruminants (PPR) is often a fatal viral disease of sheep, goat (small ruminants) and Artiodactyla in general. PPR (goat plague) is clinically indistinguishable from Rinderpest (cattle plague). PPR is prevalent in sub-Saharan Africa, Turkey, Middle-East, Iraq, Iran, and the entire Indian sub-continent. The causative agent PPRV belongs to the genus Morbillivirus, family Paramyxoviridae. The morbilliviruses, comprising important vertebrate pathogens, form a serologically cross-reactive, monotypic, closely related genus in the family Paramyxoviridae, order Mononegavirales. Lack of neuraminidase activity on the cell-attachment protein, hemagglutinin (H) of Morbilliviruses has been used as a classification parameter to differentiate Morbilliviruses from other genus under Paramyxoviridae.[1] The surface glycoproteins mediate virus–host interaction and cell-to-cell spread of virus. They play an important role in causing successful viral infection and spread. The H protein is the most variable among all the members of the Morbillivirus and this could be due to immune selection. This study was initiated in order to characterize biological activities of PPRV H protein and to assess the variation in the virus. A study of the variation would lead to a better understanding of the molecular basis of the PPRV virulence, role of immune selection in virus evolution, host specificity, type of viruses in circulation, rationalize design, and choice of vaccines and development of novel therapies.

2. Experimental

The work is divided into two major parts. The first part deals with the characterization of the biological activities associated with the H protein, elucidation of sequence determinants for PPRV H protein to function as cell-attachment protein. The second part of the work involves RT-PCR amplification, cloning, and sequencing of the H gene from various PPRV isolates. The data thus generated were employed to assess phylogenetic relationships among the various isolates of PPRV presently prevalent across the globe.

3. Results and discussion

3.1. *PPRV H is an HN*

The ability of the PPRV to adsorb red blood cells (RBCs) and further agglutinate them, a hitherto unknown biological activity, hemagglutination (HA), has been studied in detail using the prototype Indian isolate of PPR Ind TN 87/1. Further, the receptor-destroying enzyme (RDE) activity has been shown for the purified PPRV. The PPRV RDE bears similarities to New Castle Disease Virus (NDV) RDE. The erythrocyte receptor-destroying activity is not shared with Measles virus (MV), suggesting that the erythrocyte receptor for PPRV is not a protein molecule.[2] The results reported in this work suggest that a sialoglycoprotein or a sialoglycoprotein-

conjugate may be the erythrocyte receptor for PPRV. The RDE for PPRV has been shown to be a neuraminidase (NA) and conclusively proven by showing NA activity with purified H protein, which also shows HA activity. Thus, the PPRV H protein is a hemagglutinin-neuraminidase (HN). From deduced amino-acid sequence of PPRV H and comparison with the recently predicted 3D structure of the HN and Morbillivirus H proteins, the PPRV H residues topologically equivalent to HN and Influenza NA active-site residues have been identified.

3.2. *Phylogenetic analysis of PPRV based on the hemagglutinin–neuraminidase (HN) gene and protein sequences*

The H gene of various PPRV isolates was amplified by RT-PCR and the products were cloned. PCR products corresponding to 2.0 kb (the full length H gene) were obtained for 8 African and 3 Indian isolates. Complete sequence of both the strands was determined. Partial amplification of the H gene could be achieved for 4 Indian isolates and their sequence was also determined. A large single open-reading frame in the H gene encodes the 609 amino-acid-long H protein. The H protein is a type II surface glycoprotein, with the hydrophobic transmembrane domain at the amino terminus of the protein. Multiple sequence alignments were computed to estimate distances. The distance data obtained was corrected using Kimura-2 parameter method and Gamma distances using the MEGA software for reconstructing phylogenetic relationships. The distances were grouped according to the neighbor-joining method. Bootstrap analysis was performed to estimate the robustness of the grouping of the clades. Based on such rigorous phylogenetic analysis the relationships between various circulation isolates of PPRV were reconstructed.

Both NA and HA activities were conclusively demonstrated using the purified PPRV H protein. In the PPRV H-deduced amino-acid sequence, residues corresponding to viral neuraminidase active site could be identified. The 2D model generated for PPRV H using various secondary structure prediction methods was folded into 3D using homologous MV-H monoclonal antibody epitope data. With the determination of molecular and biochemical basis of PPRV H neuraminidase activity, the use of the property 'lack of neuraminidase activity' as a parameter to group viruses under Morbillivirus should be discontinued. The H gene showed scattered variation of up to 13.4% at the nucleotide and 9.4% at the amino-acid level. The mutation rate in the PPRV H gene was estimated to be 6.65×10^{-5} substitutions per nucleotide position. Predominant occurrence of amino acid changes whenever there is a nucleotide change demonstrates the role of immune selection in the evolution of the virus. The extent of variation observed in PPRV is similar to that observed for RPV or CDV. Unlike RPV, the PPRV isolates grouped into four different lineages are not always geographically restricted. No epidemiological center could be identified for PPR in Africa or India. The number of PPRV lineages in Africa is four while that in India is only three.

References

1. PRINGLE, C. R. The order Mononegavirales: evolutionary relationships and mechanisms of variation. In *Molecular basis of virus evolution* (A. J. Gibbs, C. H. Calisher and F. Garcia-Arenal, eds), Cambridge University Press, 1995, Vol. 29, pp. 426–437.

2. RAMACHANDRAN, S., SHAILA, M. S. AND SHYAM, G. Hemagglutination and hemadsorption by Peste des petits ruminants virus (PPRV), Immunobiology of virus infections, *Proc. 3rd Congress Eur. Soc. Vet. Virol.* (M. Schwayzer *et al.*, eds), 1995, pp. 513–515.

Thesis Abstract (Ph. D.)

Characteristics of growth inhibition of human promonocytic leukaemic U937 cells by interferon gamma by Joshi Chirag Vinaychandra
Research supervisor: Prof. P. Ajit Kumar
Department: Molecular and Cellular Biology

1. Introduction

Interferon gamma (IFN-γ) exerts a variety of biological effects, which include inhibition of cell proliferation, immunomodulation, induction of antiviral state, apoptosis, and differentiation.[1] The IFN is believed to mediate these pleiotropic effects through the modulation of expression or activity of a variety of genes and proteins. Binding of IFN-γ to its specific receptor on the cell surface initiates a cascade of events, which result in the activation of the latent cytoplasmic transcription factor, STAT 1α through phosphorylation. The phosphorylated STAT 1α migrates to the nucleus and binds to Gamma-IFN Activation Sequences (GAS), which are present upstream to the IFN-inducible genes, leading to their expression.[2] Although several intracellular changes that occur in response to IFN-γ have been studied, the exact mechanism by which the IFN arrests proliferation of cells is not yet known. This work is an attempt to characterize the nature of IFN-γ-mediated growth arrest of human promonocytic leukaemic U937 cells. Previous studies from this laboratory have shown that IFN-γ inhibits the growth of nontransformed, human amniotic WISH cells by arresting cell cycle progression at the G1/S boundary in a reversible manner.[3] In the present, but parallel study, investigation was focussed on the growth inhibitory action of the IFN on the human promonocytic leukaemic U937 cells, a transformed cell line unlike WISH. The study was undertaken with the objective of finding out whether the growth inhibitory action of IFN-γ on a transformed cell line such as U937 would be similar to that exerted on the nontransformed WISH cells. Therefore, the principal goals of this study were to determine: (i) whether the growth inhibition of U937 cells by IFN-γ occurred in a cell-cycle phase-specific manner; (ii) whether the arrest of proliferation was reversible, and (iii) the characteristics of the growth arrest of U937 cells by IFN-γ.

2. Results and discussion

U937 cells were confirmed to be sensitive to the growth inhibitory effect of IFN-γ at a minimum concentration of 100 units/ml by the determination of viable cell number using the trypan blue dye exclusion method. The cells were found to get growth-arrested from the 24th hour of treatment onwards. Viable cell count of the cells, which were released from 48 hours of IFN treatment (after complete growth inhibition), did not show any increase indicating that the growth inhibition was not reversible unlike in the case of WISH cells. This observation was confirmed by the finding that the cells, which were released from growth inhibition, did not incorporate ^{3}H-thymidine over a time period of 48 hours after release, indicating the

lack of fresh DNA synthesis. Bivariate flow cytometry based on fluorescence of 5-bromo-2-deoxyuridine-incorporated DNA, which was counterstained with propidium iodide, revealed that, unlike in WISH cells, growth arrest of U937 cells was not specific to any phase of the cell cycle. It also showed that with increase in the duration of IFN-γ treatment from 48 to 72 hours, there was a progressive decrease in the fraction of actively cycling cells in the S-phase from about 4% to 0.33%, respectively. A series of inhibitors, known to arrest the cell cycle in specific phases, was used to arrest the U937 cells in different phases so that the effect of IFN-γ can be studied on the synchronized population. However, the growth inhibitory effect of these inhibitors was irreversible, and hence, this line of experimentation could not be followed.

Since U937 cells are quasidifferentiated myeloid cells, it was likely that IFN treatment led to the induction of terminal differentiation resulting in an irreversible arrest of proliferation. In other words, growth arrest might have been a consequence of the induction of terminal differentiation, as the two phenomena are mutually exclusive. In order to verify this possibility, several parameters, such as morphological changes, respiratory metabolic changes, and biochemical changes, were used to monitor for myeloid differentiation. Phorbol-12-Myristate-13-Acetate (PMA), which is known to induce terminal differentiation in U937 cells, was used as the positive control. While PMA treatment did bring about terminal differentiation-related morphological changes in U937 cells, IFN-γ treatment did not result in any of such changes. Similarly, biochemical changes such as generation of free radicals and reducing power as monitored by nitro blue tetrazolium reduction could be observed upon treatment of U937 cells with PMA but not with the IFN. Treatment of cells with PMA and IFN together brought about all the above changes in a much shorter period. Thus it was established that IFN-γ treatment does not effect terminal differentiation on its own in U937 cells. However, the presence of IFN-γ along with PMA was to hasten the PMA-mediated terminal differentiation process.

Another possible reason for the lack of resumption of growth could be that IFN-γ might have induced apoptotic or necrotic cell death. Several parameters such as trypan blue and propidium iodide dye exclusion, DNA laddering, Hoechst 33342 and propidium iodide dual-staining of cells, and flow cytometric determination of mitochondrial transmembrane potential, were used to find out this possibility. Etoposide VP-16, a known inducer of apoptosis in U937 cells, was used as the positive control in these experiments. Although about 30% of the cell population could undergo some of the changes associated with apoptosis and necrosis, majority of the population did not show any such changes. This indicated that the irreversibility of inhibition of growth of U937 cells by IFN-γ was not due to induction of cell death.

The growth-arrested cells, which were released from IFN-γ block, could not be stimulated to proliferate by enriched growth medium or by co-culture with untreated cells. However, these cells could be induced to undergo differentiation or apoptosis using PMA or etoposide, respectively. The rate of protein synthesis in IFN-mediated growth-arrested cells was reduced by 40%. These results indicated that probably IFN-γ treatment had effected a state of quiescence in U937 cells from which they can be induced to differentiate or die, but cannot be induced to resume proliferation.

Simultaneous study on the possible modulation of expression of genes such as cyclins, cdks, cdk inhibitors, tumour suppressors, and so on, that are likely to be involved in growth regulation, did not show significant changes in the Northern analysis of total RNA derived

from growth-arrested cells. However, Rb gene was found to be upregulated by 1.7 fold in 12–24 h of IFN-γ treatment. Unlike in other reported systems, p21 was not upregulated in U937 cells following IFN-γ treatment.

The observations made for U937 cells are strikingly different from those made for WISH cells which are arrested by IFN-γ in a reversible, cell-cycle phase-specific manner at the G1/S boundary. The induction of quiescence could represent a novel mechanism for the inhibition of proliferation by IFN-γ.[4]

References

1. PESTKA, S., LANGER, J. A., ZOON, K. C. AND SAMUEL, C. E. — Interferons and their actions. *A. Rev. Biochem.*, 1987, **56**, 727–757.
2. DARNELL, J. E. Jr. — STATs and gene regulation, *Science*, 1997, **277**, 1630–1635.
3. SUPRIYA, P., JOSHI, C. V. AND AJITKUMAR, P. — IFN-γ inhibits growth of WISH cells in a cell cycle phase-specific manner, *J. Interferon Cytokine Res.*, 1998, **18**, 215–218.
4. JOSHI, C. V., SUPRIYA, P. AND AJITKUMAR, P. — Growth inhibition of human promonocytic leukaemic U937 cells by interferon gamma is irreversible and not cell cycle phase-specific, *Cytokine*, 1999, **11**, 673–678.

Thesis Abstract (Ph.D.)

Genetic manipulation of tomato (*Lycopersicon esculentum* Mill.) for virus resistance by
C. S. Sree Vidya
Research supervisor: Prof. G. Lakshmi Sita
Department: Microbiology and Cell Biology

1. Introduction

Tomato belongs to the family Solanaceae and is considered a very important vegetable crop worldwide. Tomato plants are severely infected with several viruses, bacteria, fungi, nematodes and insects leading to tremendous crop loss. Conventional breeding techniques to obtain disease resistance are too laborious and inadequate. To introduce desired gene or a set of genes by conventional breeding requires a sexual cross between two lines and then repeated back crossing between the hybrid offspring and one of the parents until a plant with the desired characteristic is obtained. Production of disease-resistant plants by genetic engineering has increased to obtain resistance against insects, fungi, bacteria, virus and nematodes. The present study was initiated with the aim of genetically manipulating tomato plants to produce disease-tolerant plants. Two approaches are adapted. One is by overexpressing defense-related genes, which are expressed during infection called pathogenesis-related (PR) genes to obtain broad range resistance. It has been reported that in many plants overexpression of defense-related genes like chitinase,[1] coexpression of chitinase and glucanase, polygalacturonase inhibitor[2] brings protection against disease. The second approach is the pathogen-derived resistance which involves transferring the part of the viral genome-like coat protein (CP),[3] movement protein[4] and altered form of replicase[5] to obtain viral resistance.

We have undertaken both the above-mentioned approaches to obtain disease-resistant plants. Coat protein gene (CP) of Physalis mottle virus (PhMV) (provided by Dr Savithri *et al.*) was used to obtain pathogen-derived resistance in tomato plants. Pathogenesis-related gene from tomato has been cloned to obtain host-mediated resistance. These results are presented here.

2. Experimental

2.1. *Cloning and characterization of disease-resistance gene*

To clone pathogenesis-related (PR) genes from tomato, tomato leaves were treated with salicylic acid (SA) to induce PR genes. Total RNA was isolated and mRNA was purified. cDNA library was constructed in λMOSElox (Amersham) vector system. Recombinant plaques were subcloned to plasmid MOSElox by automatic subcloning and random analysis of cDNA library was performed. Putative recombinant plasmids of size 700 bp to 1 kb were further taken for sequence analysis which led to the identification of full-length 700 bp intracellular PR (IPR) gene and named as TSI-1 (tomato stress induced-1). The deduced amino-acid sequence of TSI-1 codes for a 178 amino-acid polypeptide with a 534 bp open reading frame starting with the first translation initiation codon ATG at position 40 and ending with a stop codon TAA at position 574. TSI-1 is acidic and the calculated isoelectric pH is 5.8. Its predicted molecular weight is 20.4 kDa. TSI-1 shows maximum homology to potato IPR genes, i.e. 71% to STH-2 and STH-21 at nucleotide level which are expressed against fungal infection, 30%–40% with the tree pollen allergens and other IPR members from soybean, pea, bean, alfalfa, lily, carrot and asparagus. Tomato genomic DNA was digested with various restriction enzymes and subjected to Southern analysis which revealed that TSI-1 belongs to multigene family like other reported IPR members. Northern analysis was performed to analyze the induction pattern of TSI-1 for SA. The levels of TSI-1 transcripts increased as the concentration of SA increased and were maximal at 10 mA SA after 48 hours. TSI-1 was not expressed for water treatment and an extremely faint signal was obtained for mild concentration of SA. Expression was very well correlated with the concentration of SA, which indicates that SA induces expression of TSI-1. After stripping and reprobing with 18S rRNA, similar signal intensities were obtained which indicates equal loading of RNA in all lanes. Northern analysis was performed with RNA isolated from *Fusarium oxysporum* fungal-treated tomato leaves and fresh tomato leaves as control. Highly intense signals were obtained in fungal-treated leaves after exposure for 24 h but no transcripts were detected in fresh tomato leaves even after exposure for 2 days.

2.2. *Genetic transformation of tomato with Physalis mottle virus coat protein (PhMV CP)*

Tomato plants are infected by many viruses and PhMV virus is one among them. Tomato plants infected with PhMV develop chlorotic and necrotic symptoms and hampers the growth of plants. Viral resistance was obtained by genetic transformation of tomato with CP gene of PhMV through *Agrobacterium*-mediated transformation.

Initially, efficient regeneration was obtained through organogenesis by culturing two-week old cotyledonary leaves on the MS medium (MS) supplemented with 0.5 mg/l thidiazuron (TDZ). After 3 weeks, the callus which appeared at the cut ends was subcultured on the fresh

MS medium with 0.5 mg/l TDZ for differentiation into shoot buds. The shoot buds elongated to shoots in the same regeneration medium and subsequently transferred to half MS medium supplemented with 0.5 mg/l indole acetic acid (IAA) for root induction. Fully regenerated plants were transferred to soil after acclimatization in tissue culture conditions. After establishing regeneration system, *Agrobacterium*-mediated transformation was standardized using GUS marker genes. Tomato leaves were transformed with pBI121 binary vector and transgenic plants were selected for kanamycin resistance (50 mg/l) and the transformed plants were subjected to GUS assay and PCR analysis using *npt II* gene-specific primers to amplify 700 bp fragment of *npt II*. After establishing the transformation with GUS, marker gene tomato plants were transformed with the coat protein gene of PhMV. CP gene of PhMV was cloned into pBI121 binary vector under CaMV 35S promoter by deleting GUS gene and transformed to *Agrobacterium* by freeze thaw method and tomato was transformed with CP gene using the same conditions that were used to transfer GUS gene of pBI121 vector. Transformed shoots were screened for kanamycin resistance phenotype and subjected to molecular analysis. 600 bp fragment of CP gene was amplified using CP gene-specific primers. Southern blot analysis revealed the integrity of the transgene in tomato genome. Total proteins were extracted and Western blot analysis was performed using monoclonal antibodies to CP. All the transgenic plants showed expression of CP protein. T_0 plants were self-pollinated to produce fruits. T_1 seeds were sown in green house and challenged with PhMV to characterize the degree of resistance obtained due to CP expression by observing symptom development.

3. Discussion

Representative SA-induced cDNA library was constructed in λMOSElox vector system. Random analysis of recombinant plasmids revealed the presence of tomato TSI-1. Southern blot analysis revealed TSI-1 is a member of a gene family. They occur as multigene families in potato, carrot, alfalfa, soybean, potato and pollen allergens to which it shows considerable homology. IPR genes are reported to express during stress conditions like pathogen invasion, wounding, arachidonic acid and absicisic acid treatment. Exogenous application of SA induces PR genes in many systems and they act as pathogenic signals. Exogenous application of SA clearly shows that SA has significant induction over TSI-1. We would see less-intense signal after treatment with SA for 12 h at 1 mM and the expression increased as the concentration of SA increased and clear signals were obtained in all the SA-treated leaves. RNA was isolated from fresh leaves and probed with TSI-1 to check the constitutive expression of TSI-1, which did not give detectable signal in Northern analysis. It behaves like any other SA response genes expressed during hypersensitive reaction. The function of this TSI-1 remains unknown. A stretch of amino acids from 83rd to 126th of TSI-1 which is considered as the signature motif had homology with the structurally related *Bet VI*-type pollen allergens and other related IPR proteins from plants. The recent reports on white birch pollen and grass allergens are known to have RNase activity. It could be possible that TSI-1 may be involved in degrading invading pathogenic RNA. We conclude that tomato IPR is a low-molecular-weight protein expressed against stress. It is organized as a gene family in tomato genome and highly inducible by salicylic acid. This gene can be overexpressed in tomato to obtain broad-range resistance against pathogens. The nucleotide sequence data reported will appear in EMBL nucleotide sequence database under the accession number Y15846.

As a second strategy to develop resistant plants, transformation of tomato plants harboring PhMV CP gene was achieved. This is the first report on tomato (Indian variety) showing resistance to PhMV (tymo viral group). Regeneration on tomato was attempted to obtain quick and efficient protocol, which can be used for further transformation experiments. Several plant-growth hormones were tried using different explants such as cotyledons, hypocotyl and leaves for regeneration. Among the several cytokinins and auxins tried best regeneration was obtained in 0.5 mg/l of TDZ. Cotyledonary leaves inoculated in MS medium supplemented with 0.5 mg/l TDZ gave high number of shoots (5 per explant). Established plants were obtained within a period of 3 months. Standardization of transformation was carried out by *Agrobacterium*-mediated transformation harboring pBI121 binary vector. Transformation of tomato with pBI121 binary vector was carried out to standardize the conditions suitable for tomato transformation. Initial standardization was carried out with the GUS reporter gene. Only the transgenic plants showed GUS activity showing blue colour and the control plants were colourless showing absence of GUS activity and it is specific in transgenics due to integration of GUS gene. Further confirmation was done by PCR analysis using *npt II* gene-specific primers. Expected 700 bp size products were obtained showing further confirmation of integrated T DNA in the tomato genome. Out of 20 plants growing in kanamycin medium, we obtained 6 independently regenerated T_0 plants expressing high-level CP protein. Transgenic nature was confirmed by molecular analysis such as PCR and Southern hybridization. Intensity and pattern of integration varied among plants showing the occurrence of random integration. All the T_1 plants analyzed showed the same level of CP expression. Southern and ELISA analysis were undertaken in T_1 plants to check the successful inheritance of CP. Interestingly, Southern analysis showed a similar pattern of signals for plants originating from a single fruit. ELISA results showed that out of 30 plants analyzed, 20 expressed CP that is close to the Mendelian segregation ratio of 3:1. The 20 plants inoculated with the virus initially showed low levels of virus accumulation but virus titer increased 30 days after inoculation. Twelve out of 20 plants developed symptoms as control plants. In 8 of the transgenic plants, the infection was however restricted to local lesions (chlorotic spots) on the inoculated leaves only. These plants expressed high levels of CP initially. In some of the low CP-expressing plants, systemic infection was avoided by cutting primary leaves. Transgenic plants expressing low levels of CP accumulated more virus compared to transgenics which expressed high-level CP and the virus titer was low compared to nontransgenic plants. It is possible that the constitutively expressed CP which forms the capsid blocks the site for disassembly of inoculated virus and ribosome binding to undergo initial translation needed for replication. The possibility of CP RNA interacting with the negative strand of the replicating virus to interfere virus replication cannot be ruled out since tobacco plants transgenic to PhMV CP were symptom free after infecting with PhMV RNA (Ranjit *et al.*, unpublished report). This can be applied to tomato since both tomato and tobacco belong to Solanaceae. This method can be exploited for frequent and successful production of transgenic plants harboring other CP gene and pathogen-derived genes of harmful viruses to produce disease-resistant plants.

References

1. Broglie, K. *et al.* *Science*, 1991, **254**, 1194–1197.

2. Zhu, Q. *et al.* *Biotechnology*, 1994, **12**, 807–812.

3. POWELL, A. L. T. *et al.* In *Advances in molecular genetics of plant–microbe interactions*, Vol. 3, (M. Daniels *et al.* eds), Kluwer Academic, 1994, pp. 399–402.

4. SANFORD, J. C. AND JOHNSON, S. A. *J. Theor. Biol.*, 1985, **113**, 395–405.

5. SEPPANEN, P. *et al.* *J. Gen. Virol.*, 1997, **78**, 1241–1246.

6. WINTERMANTEL, W. M. *et al.* *Virology*, 1997, **231**, 248–257.

Thesis Abstract (Ph. D.)

Synthetic, spectroscopic and structural investigations on homo- and heterodinuclear transition metal complexes of diphosphinoamine ligands, $MeN\{P(OR)_2\}_2$ ($R = CH_2CF_3$ or C_6H_5) by M. Ganesan

Research supervisor: Prof. S. S. Krishnamurthy
Department: Inorganic and Physical Chemistry

1. Introduction

Diphosphinoamines of the type $RN\{PX_2\}_2$ (R = alkyl or aryl; X = F, Cl, alkyl, aryl, alkoxy or aryloxy) are versatile ligands capable of forming a variety of complexes with transition metals in which they exhibit chelating, bridging and monodentate modes of coordination.[1–5] In the present investigation, several new aspects of the organometallic chemistry of diphosphinoamine ligands bearing electron-withdrawing substituents, $MeN\{P(OR)_2\}_2$ ($R = CH_2CF_3$, **L1** or C_6H_5, **L2**) have been explored. The topics investigated are: (1) Reductive carbonylation of $CoCl_2$, (2) Synthesis of Group 10 metal complexes, and (3) Synthesis of Pd-Mo and Ni-Mo heterometallic complexes.

2. Results and discussion

2.1. *Reductive carbonylation of $CoCl_2$ in the presence of diphosphinoamines*[6]

Reduction of $CoCl_2$ by $NaBH_4$ in ethanol in the presence of $MeN\{P(OR)_2\}_2$($R = CH_2CF_3$) and carbon monoxide at one atmospheric pressure gives an unusual mononuclear complex, $[Co(CO)\{P(OR)_2(NHMe)\}_2\{P(O)(OR)_2\}\{P(O)(OR)_2\}\{P(H)(OR')_2\}]$, ($R = CH_2CF_3$, $R' = CH_2CH_3$) (**1**) formed by cleavage of a P–N bond and by *trans*-esterification. When the reductive carbonylation is carried out by using Zn as the reducing agent in the presence of the diphosphazanes, $MeN\{P(OR)_2\}_2$ ($R = CH_2CF_3$ or C_6H_5), the complexes $[Co_2(CO)_2(\mu\text{-}MeN\{P(OR)_2\}_2)_3]$ ($R = CH_2CF_3$) (**2**), $[Co_2(CO)_4(\mu - MeN\{P(OR)_2\}_2)_2]$ ($R = C_6H_5$) (**3**), $[Co(CO)(\eta^2 - MeN\{P(OR)_2\}_2)_2][CoCl_3(thf)]$ ($R = C_6H_5$) (**4**) are isolated.

2.2. *Group 10 metal complexes*

Treatment of NiI_2 with $MeN\{P(OR)_2\}_2$ ($R = C_6H_5$ or CH_2CF_3) gives the mononuclear $[NiI_2(\eta^2\text{–}MeN\{P(OR)_2\}_2)]$ ($R = C_6H_5$) (**5**) and dinuclear $[Ni_2I_2(\mu\text{–}I)_2(\mu\text{–}MeN\{P(OR)_2\}_2)_2]$ ($R = CH_2CF_3$) (**6**) complexes respectively. The reactions between $MeN\{P(OR)_2\}_2$ ($R = CH_2$

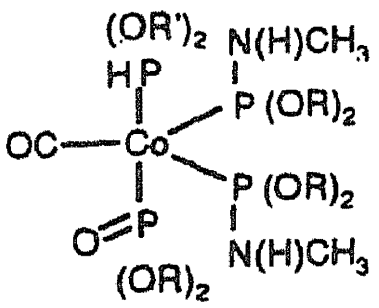

1*, R = CH_2CF_3
R' = CH_2CH_3

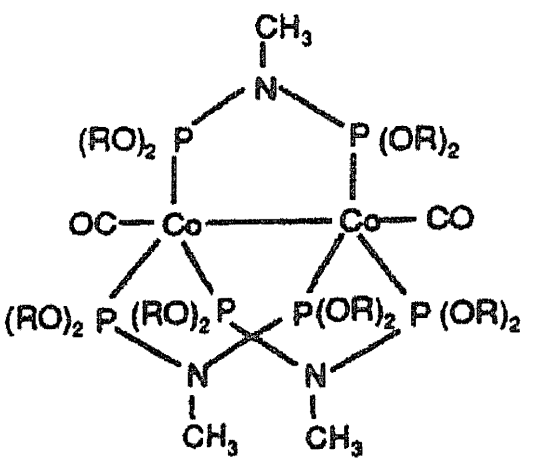

2*, R = CH_2CF_3

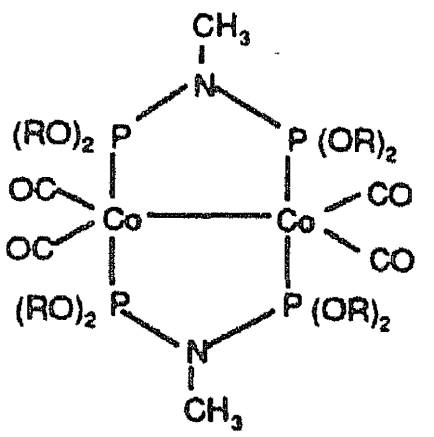

3, R = Ph

CF_3) and $[Pd(COD)Cl_2]$ and $[Pt(COD)Cl_2]$ give $[Pd_2Cl_2(\mu\text{–}MeN\{P(OR)_2\}_2)_2]$ (**7**) and $[Pt\{P(O)(OR)_2\}_2\{P(OR)_2(OH)\}_2]$ (**8**) respectively. The dipalladium(I) complex $[Pd_2I_2(\mu\text{–}MeN\{P(OR)_2\}_2)_2]$ (R = C_6H_5) (**9**) is obtained by a redox reaction between (**5**) and $[Pd_2(\mu\text{–}MeN\{P(OR)_2\}_2)_3]$ (R = C_6H_5).

2.3. *Palladium–molybdenum and nickel–molybdenum heterometallic complexes*[7]

The reaction of **5** with $[Mo_2(\eta^5\text{–}C_5H_5)_2(CO)_6]$ gives the heterodinuclear complex $[(\eta^5\text{–}C_5H_5)Mo(I)(\mu\text{–}I)(\mu_{sb}\text{–}CO)(\mu\text{–}MeN\{P(OR)_2\}_2)NiI]$ (R = C_6H_5) (**10**) and the mononuclear complex $[(\eta^5\text{–}C_5H_5)Mo(CO)I(\eta^2\text{–}MeN\{P(OR)_2\}_2)]$ (R = C_6H_5) (**11**). The reactions of the dipalladium complexes $[Pd_2Cl_2(\mu\text{-}MeN\{P(OR)_2\}_2)_2]$ (R = CH_2CF_3 or C_6H_5) with $[Mo_2(\eta^5\text{–}C_5H_5)_2(CO)_6]$ in boiling benzene give Mo-Pd dinuclear and $MoPd_2$ trinuclear complexes $[(\eta^5\text{–}C_5H_5)(CO)Mo(\mu\text{–}MeN\{P(OR))_2\}_2)_2PdCl]$ (R = CH_2CF_3 or C_6H_5) (**12**), $[(\eta^5\text{–}C_5H_5)Mo(\mu_{3sb}\text{–}CO)_2(\mu\text{–}MeN\{P(OR)_2\}_2)_2Pd_2Cl]$ (R = CH_2CF_3 or C_6H_5) (**13**) and $[(\eta^5\text{–}C_5H_5)(Cl)Mo(\mu_{sb}\text{–}CO)(\mu\text{–}Cl)(\mu\text{–}MeN\{P(OR)_2\}_2)PdCl]$ (R = CH_2CF_3 or C_6H_5) (**14**) as well as the Mo(II) complexes $[(\eta^5\text{–}C_5H_5)Mo(CO)Cl(\eta^2\text{–}MeN\{P(OR)_2\}_2)]$ (R = CH_2CF_3 or C_6H_5) (**15**) which can be separated by column chromatography. The reaction between $[Mo_2(\eta^5\text{–}C_5H_5)_2(CO)_6]$ and $MeN\{P(OR)_2\}_2$ (R = C_6H_5) in boiling toluene gives the dimolybdenum complex, $[Mo_2(CO)_4(\eta^5\text{–}C_5H_5)_2(\eta^1\text{–}MeN\{P(OR)_2\}_2)_2]$ (R = C_6H_5) (**16**).

The complexes have been characterized by C, H, N elemental analysis and IR and NMR spectroscopic data. The structures of **1**, **2**, **4**, **6**, **7**, **8**, **10**, **12a**, **13b**, **14a** and **15b** have been confirmed by single-crystal X-ray diffraction studies.

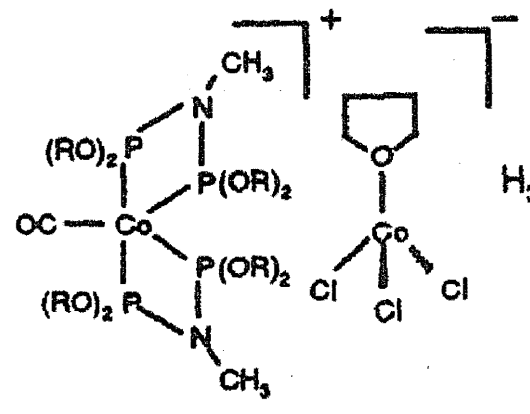

4*, R = Ph

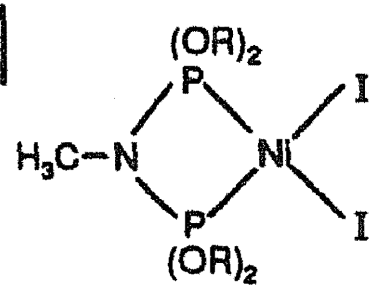

5, R = Ph

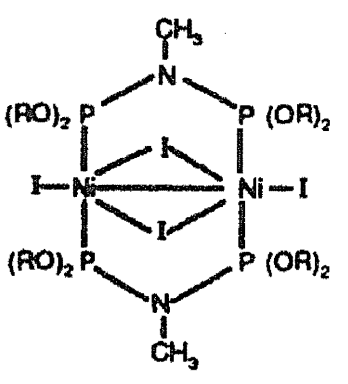

6*, R = CH_2CF_3

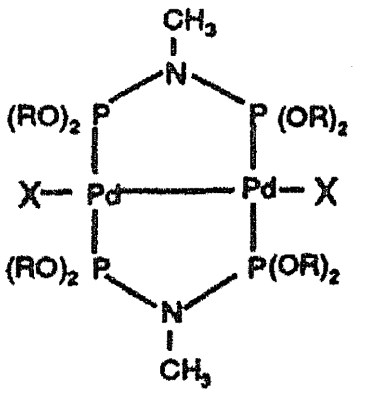

7*, R = CH_2CF_3; X = Cl
9, R = Ph; X = I

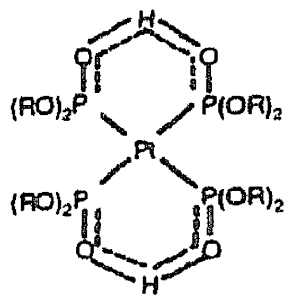

8*, R = CH_2CF_3

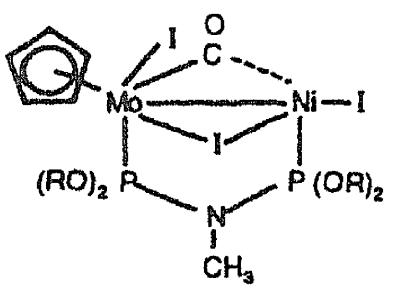

10*, R = Ph

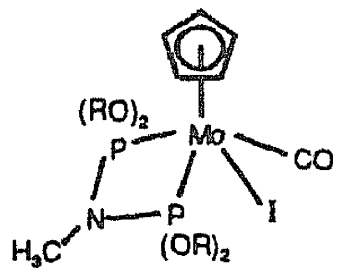

11, R = Ph

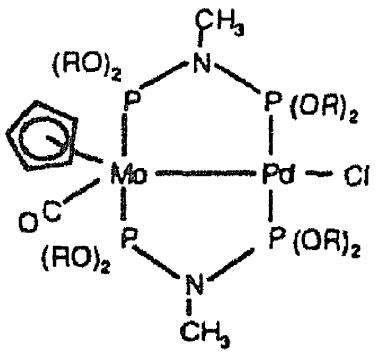

12a*, R = CH_2CF_3
12b, R = Ph

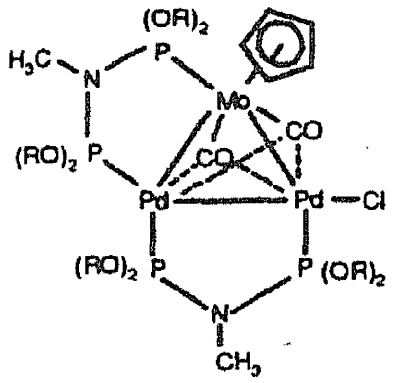

13a, R = CH_2CF_3
13b*, R = Ph

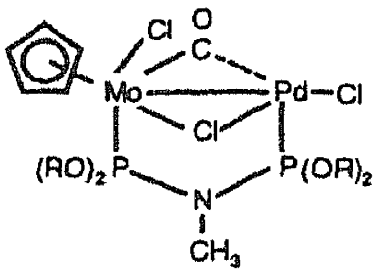

14a*, R = CH_2CF_3
14b, R = Ph

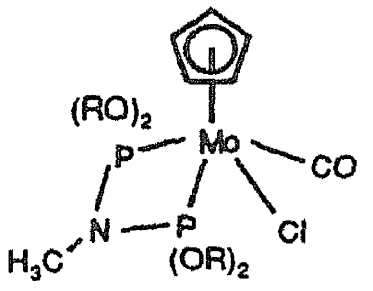

15a, R = CH_2CF_3
15b*, R = Ph

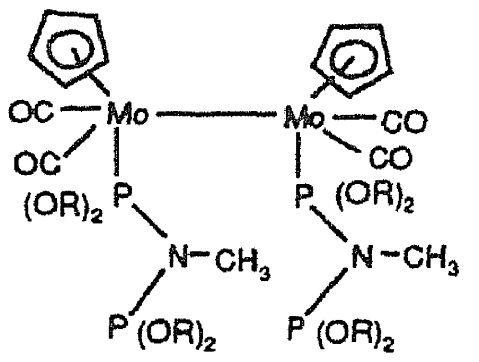

16, R = Ph

3. Experimental

All the reactions were carried out using standard Schlenk-line techniques and solvents were purified prior to use. The ligands **L1** and **L2** were synthesised by the treatment of $MeN(PCl_2)_2$ with CF_3CH_2OH and C_6H_5OH in the presence of Et_3N in diethylether. Metal precursors such as $[Mo_2(\eta^5\text{–}C_5H_5)_2(CO)_6]$ and $[Pd_2Cl_2(\mu\text{–}\mathbf{L2})_2$ were prepared by literature procedures. The NMR spectra were recorded using Bruker AMX-400 or ACF-200 spectrometers. Single-crystal X-ray diffraction data were collected using Enraf-Nonius CAD-4 diffractometer.

4. Conclusions

The results obtained in the present investigation demonstrate the considerable scope and versatile nature of diphosphazane ligands for the synthesis of a range of transition metal complexes, in particular heterodi- and trinuclear complexes. Significant differences in the reactivities and the structural features of the resulting complexes are observed between the two ligands $MeN\{P(OR)_2\}_2$ ($R = CH_2CF_3$ or C_6H_5). The trifluoroethoxy-substituted ligand shows a more pronounced tendency to form bridging type of complexes rather than of chelate type formed by the phenoxy-substituted ligand. The structural data on the complexes show that the mean M–P distances are shorter than those found in dppm or dppe complexes. This trend is in support of strong π-acceptor nature of the ligands which is also reflected in the magnitude of carbonyl-stretching frequencies observed for these complexes. The P–N distances fall in the range 1.63–1.68 Å and are shorter than the accepted value for a P–N single bond distance (1.77 Å) found in $H_3N^+\text{–}PO^-_3$. The mean P–N–P angles of the bridging diphosphazanes vary from 113 to 122°; in the chelate complexes, the mean P–N–P angles are 96–97°. In spite of this large variation in the P–N–P angles, the planarity around the nitrogen is maintained in all cases as observed in numerous other diphosphazane complexes. The structural data for complexes

containing semibridging carbonyl ligands throw much light on the nature of metal–metal interactions.

References

1. BALAKRISHNA, M. S., REDDY, V. S., KRISHNAMURTHY, S. S., NIXON, J. F. AND BURCKETT ST LAURENT, J. C. T. R. — *Coord. Chem. Rev.*, 1994, **129**, 1.
2. WITT, M. AND ROESKY, H. W. — *Chem. Rev.*, 1994, **94**, 1163.
3. BHATTACHARYYA, P. AND WOOLLINS, J. D. — *Polyhedron*, 1995, **14**, 3367.
4. KRISHNAMURTHY, S. S. — *Proc. Indian Acad. Sci. (Chem. Sci.)*, 1996, **108**, 111.
5. KING, R. B. — *Acc. Chem. Res.*, 1980, **13**, 243.
6. GANESAN, M., KRISHNAMURTHY, S. S. AND NETHAJI, M. — *J. Organomet. Chem.*, 1998, **570**, 247.
7. GANESAN, M., KRISHNAMURTHY, S. S., NETHAJI, M. AND RAGHURAMAN, K. — Paper presented at the Poster Section of *XIV-Int. Conf. on Phosphorus Chemistry*, Cincinnati, Ohio, USA, July 12–17, 1998.

Thesis Abstract (Ph. D.)

Resonance Raman studies on structure and dynamics of azobenzene and its derivatives

by Nandita Biswas
Research supervisor: Dr. Siva Umapathy
Department: Inorganic and Physical Chemistry

1. Introduction

Resonance Raman (RR) spectroscopy has become a widely used technique to probe the structure and dynamics of short-lived excited state intermediates of various photochemical and photophysical processes.[1, 2] Under pre-resonance or resonance conditions, i.e. when the excitation wavelength approaches or coincides with a particular electronic transition of the system under investigation, the RR intensities essentially contain information about the excited state potential energy surface and hence, in turn, can dictate the initial dynamics of nuclear motion in Franck–Condon (FC) region on that surface. Wavelength dependence of the Raman scattering intensity, viz. Raman excitation profiles (REPs) provide information on the origin of RR intensities and also the dynamics associated with the resonant excited state. Thus, RR spectroscopy can be used to study the initial excited state dynamics occurring in the range of tens of femtoseconds, which cannot be studied by time-resolved resonance Raman spectroscopy[3] due to the limitation resulting from broad spectral bandwidth of the laser pulse (dictated by the Uncertainty principle). This work deals with various applications of resonance Raman spectroscopy, viz. isomerization dynamics, resonance deenhancement and electron transfer reaction in azo dyes, the structure of which has attracted considerable attention, in recent times, mainly due to its wide applicability for reversible optical data storage[4] and molecular switching devices.[5] The basis for majority of these applications is the photoisomerization of azo dye[6] between the stable *trans* and the metastable *cis* conformation.

2. Experimental

In the present investigation, it is shown that the use of commercial optical parametric oscillators (OPO) enable a simple method for determining the absolute Raman cross-sections, utilizing the measurement of integrated intensity ratios.[7] Standard curves for the absolute Raman cross-sections of the commonly used internal standards, viz. acetonitrile (918 cm^{-1}), nitrate (1045 cm^{-1}), benzonitrile (1000 cm^{-1}), *n*-hexane (1454 cm^{-1}) and carbon tetrachloride (791 cm^{-1}) peaks, in the wavelength range, 450–650 nm, are presented.

3. Theoretical

A time-dependent quantum mechanical (TDQM) method of wavepacket propagation in computing RR intensities[8] for polyatomic systems is developed and presented here. The usefulness of this method is shown by applying it to *cis*-stilbene (a well-studied system). Using the TDQM technique, the absorption spectrum and the REPs of polyatomic molecules can be computed with ease and one could obtain information on the displacements in the excited state at any time after photoexcitation, but within the electronic dephasing time.

4. Results and discussion

The equilibrium structures, harmonic frequencies and mode assignments for azobenzene and its substituents are presented, since accurate vibrational analysis of the azo dyes are essential in order to understand mode-dependent structural distortions involved during the isomerization process. The vibrational analysis for *trans*-azobenzene (TAB) and *cis*-azobenzene (CAB) and their isotopic analogues[9] are presented using restricted Hartree–Fock (RHF), hybrid Hartree–Fock/density functional (HF/DF) and pure density functional theoretical (DFT) methods utilizing 6-31G* basis set. In addition, a comparative study of the equilibrium geometry and harmonic vibrational frequencies of 4-nitroazobenzene (NAB), 4-dimethylaminoazobenzene (DAB) and 4-nitro, 4′-dimethylaminoazobenzene (NDAB) using hybrid Hartree–Fock/density functional method are presented. The effect of substitution on the *para* position by an acceptor group, by a donor group and by a donor–acceptor group of the parent azobenzene molecule on the vibrational structures and harmonic frequencies is also presented.[10]

Although isomerization of azo dyes has been studied by various people in relation to the marked dependence of the photoisomerization quantum yield on excitation wavelength[6] and molecular structure, still the mechanism of isomerization in general remains a subject of controversy. The reason for this is the presence of nitrogen (N) lone pair in the azo group. Hence, in azo dyes, there are two possible routes of isomerization, namely, rotation (torsion or twist) about the central N = N bond which involves a π bond rupture and inversion (in-plane lateral shift) through a linear transition state (the π bond remaining in tact). In order to study the mechanism of isomerization under ($2^1A_g \leftarrow 1^1A_g$) electronic excitation, the REPs for the 10 Franck–Condon active fundamentals of *trans*-azobenzene in carbon tetrachloride solution are presented. It is observed that various modes of *trans*-azobenzene show reduced intensity near the maxima of the resonant electronic ($2^1A_g \leftarrow 1^1A_g$) transition.[11, 12] The observed deenhancement indicates that the resonant electronic state is not the sole source of intensity for various fundamental vibrations, instead vibronic activity arising due to preresonant state, results in deviation from the expected excitation profiles. We have used Heller's wavepacket dynamical

approach with the inclusion of interference effect from the preresonant electronic state to simulate the REPs of the Franck–Condon active normal modes. From the simulated results, we have inferred that isomerization occurs via inversion, under ($2^1A_g \leftarrow 1^1A_g$) electronic excitation. The factors leading to resonance deenhancement in *trans*-azobenzene is presented. The short-time isomerization dynamics within a few femtoseconds is examined from a priori knowledge of ground state normal mode descriptions. It is found that on ($2^1A_g \leftarrow 1^1A_g$) excitation, isomerization occurs via inversion mechanism rather than by rotation.

The concept and determination of inertial solvent reorganization energy for an intramolecular charge transfer process, using RR spectroscopy is presented.[13] These reorganization energy terms play a major role in determining electron transfer rates. RR spectra have been recorded for 4-nitro, 4′-dimethylamino-azobenzene (NDAB) within the charge-transfer transition, in a range of solvents of widely varying polarity, viz. *n*-hexane, carbon tetrachloride, benzene, acetonitrile and benzonitrile. Changes in the polarity of the solvent is thus expected to have a dramatic influence on the excited state structure and dynamics of the solute and this change in geometry, due to solvent effect, can be easily monitored using RR spectroscopy. It has been shown that RR intensities in combination with the over- and underdamped Brownian oscillator model provides a reasonable estimate to the values of solvent reorganization energy as well as mode-specific vibrational reorganization energies. From a detailed experimental and theoretical analysis of the Raman excitation profiles, it is observed that in nonpolar solvent (*n*-hexane), NDAB exists in the locally excited (LE) state whereas in other solvents, viz. carbon tetrachloride, benzene, acetonitrile and benzonitrile, it exists in the charge-transfer state. The distortions along various normal vibrations (mainly along N = N and C–N stretching coordinates) of NDAB in different solvents infer isomerization via inversion mechanism in benzene and rotation in *n*-hexane. This study indicates that the solvent polarity drastically effects the molecular structure in systems undergoing intramolecular charge transfer in the excited electronic state.

References

1. MYERS, A. B. — In *Laser techniques in chemistry* (A. B. Myers and T. R. Rizzo, eds), Wiley, 1995, Vol. 23, p. 325.
2. MYERS, A. B. AND MATHIES, R. A. — In *Biological applications of Raman spectroscopy* (T. G. Spiro, ed), Wiley, 1987, Vol. 2, p. 1.
3. HAMAGUCHI, H. — In *Vibrational spectra and structure* (J. R. Durig, ed), Elsevier, 1987, Vol. 16, Ch. 4.
4. RAMANUJAM, P. S., HVILSTED, S. AND ANDRUZZI, F. — *Appl. Phys. Lett.*, 1993, **62**, 1041.
5. SEKKAT, Z. AND DUMONT, M. — *Appl. Phys. B*, 1992, **54**, 486.
6. RAU, H. — In *Photochromism. Molecules and Systems* (H. Durr, H. Bouas-Laurent, eds) Elsevier, 1990, Ch. 4, p. 165.
7. BISWAS, N. AND UMAPATHY, S. — *Appl. Spectrosc.*, 1998, **52**, 496.
8. BISWAS, N., UMAPATHY, KALYANARAMAN, C. AND SATHYAMURTHY, N. — *Proc. Indian Acad. Sci. (Chem. Sci.)*, 1995, **107**, 233.
9. BISWAS, N. AND UMAPATHY, S. — *J. Phys. Chem. A*, 1997, **101**, 5555.
10. BISWAS, N. AND UMAPATHY, S. — Submitted.

11. BISWAS, N. AND UMAPATHY, S. *Chem. Phys. Lett.*, 1995, **236**, 24.

12. BISWAS, N. AND UMAPATHY, S. *J. Chem. Phys.*, 1997, **107**, 7849.

13. BISWAS, N. AND UMAPATHY, S. *Chem. Phys. Lett.*, 1998, **294**, 181.

Thesis Abstract (Ph.D.)

Ligand controlled reactivity in coordination chemistry: Studies on aqueous allylation, dioxygen activation and metal–metal interaction by D. Jayaprakash
Research supervisor: Prof. Ashoka G. Samuelson
Department: Inorganic and Physical Chemistry

1. Introduction

Ligands play an important role in coordination chemistry and organometallic chemistry. Coordination of the ligand to a metal ion induces a variety of physicochemical changes that result in reactions that are unique to each ligand set. The present study is focused on the role played by the ligands in three systems involving zinc-promoted allylation in aqueous media, dioxygen activation by copper and tuning metal–metal interactions in platinum dimers.

2. Aqueous allylations

The Barbier-type reaction involving the allylation of carbonyl compounds promoted by metals like Sn, In, Bi and Zn in aqueous medium provides a convenient method for C–C bond formation in organic synthesis.[1] This methodology offers relatively inexpensive, environmentally benign reaction procedures with altered selectivities. The mechanism of the Sn-, In- and Bi-promoted reactions are quite clear, while that promoted by zinc is less understood.

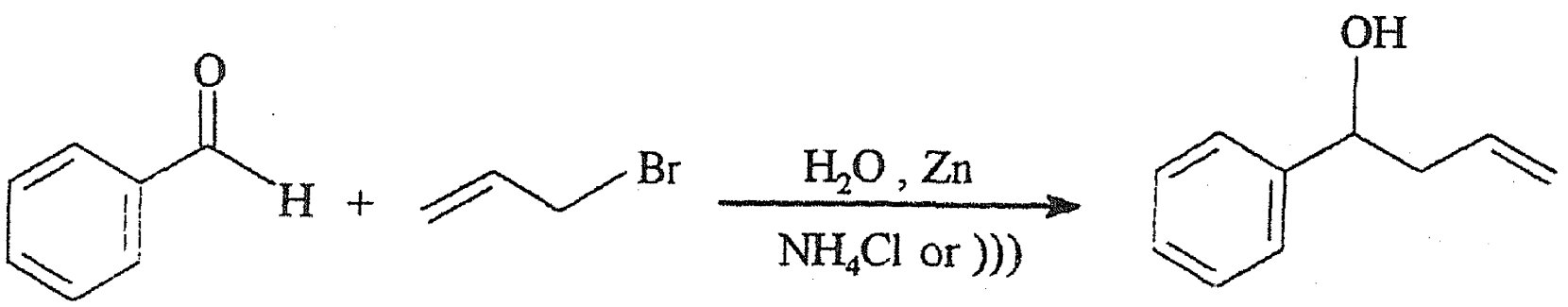

A radical species generated by a single electron transfer from the metal surface is believed to be the intermediate.[2] A complete investigation of the mechanism of the zinc-mediated allylation of carbonyl compounds in aqueous medium was carried out to understand the nature of the intermediate formed. The investigation comprises trapping and competition experiments, CO insertion and asymmetric addition.

Attempts were made to trap the intermediate with reagents that could interfere with radical as well as organometallic intermediates formed during the reaction. Control experiments without the traps were performed simultaneously to compare the yields. Reactions in the presence of radical traps like BHT, 4-tert-butylcatechol and O_2 proceed smoothly without decrease in the yield of the product alcohol suggesting that radical species may not be intermediates.

Attempts with reagents like NH_4SCN, $CBrCl_3$, NaN_3^- capable of trapping metal–carbon bonds were unsuccessful due to competing side reactions. While $CBrCl_3$ and NaN_3^- reacted with zinc in a first step, NH_4SCN reacted with the allyl halide thereby preventing the formation of the intermediate.

TEMPO is a stable-free radical known to react with both radical and metal–carbon intermediates. Reactions carried out in the presence of one equivalent of TEMPO result in a drastic decrease in the yield of the product alcohol compared to a control reaction. In the absence of benzaldehyde, TEMPO reacts with the intermediate species resulting in the formation of a colourless compound that decomposes under reaction conditions. Orange-coloured TEMPO is regenerated after the decomposotion of the trapped intermediate. A similar observation was also made in the presence of benzaldehyde which accounts for decrease in the yield of the product alcohol. As a radical pathway has been ruled out by trapping experiments with radical traps it appears likely that an allyl-zinc species is formed as the intermediate.

The reactivity of the carbonyl group could be altered by substituents present on the ring. While electron-withdrawing groups increase the reactivity, electron-releasing groups decrease it. Organozinc intermediates being electron rich would react much faster with the aldehyde having an electron-withdrawing group compared to the one with an electron-releasing group leading to the observed large difference in rates. For radical intermediates (electro- and nucleophilic), similar differences in rates of addition to substituted aldehydes would still be observed but will be of smaller magnitude.

Competition reactions between differently substituted aldehyde pairs were carried out using half equivalent of zinc and allyl halide. Aldehydes containing electron-withdrawing groups were found to react much faster than those with electron-releasing ones. In fact, *p*-hydroxy benzaldehyde failed to react with the intermediate and was recovered unreacted. However, in the absence of competing aldehydes it did react with the intermediate to give rise to the corresponding alcohol. The reactivity pattern is clearly discernible and is comparable to that observed by Zhang *et al.*[3] for the addition of diethylzinc to various substituted aldehydes. This experiment also lends support to the formation of an allylzinc intermediate.

In the presence of high pressures of CO (500–650 psi) small amounts of symmetric diallylketone was obtained. The formation of the ketone suggests the insertion of CO across the zinc carbon bond of the allylzinc intermediate.

Another interesting outcome of this investigation is the development of a methodology for asymmetric allylation. While reports on the addition of allylhalides to chiral carbonyl compounds under aqueous conditions are readily available, similar addition to achiral substrates are scarce. The only attempt with chiral auxiliaries like mannitol or camphoric acid resulted in racemic products.[4] However, in the present investigation chiral ligands like L-(+)-tartaric acid and diethyl-L-tartrate were successfully used for asymmetric induction. The stereoselectivity was found to be dependent on the reaction temperature. The chiral auxiliaries are believed to coordinate to the intermediate zinc species resulting in the formation of diastereomeric transition states whose ratio depends on the reaction temperature and is reflected in product selectivity. The observed selectivities in the presence of chiral auxiliaries could well be explained by invoking the formation of a Zn–carbon intermediate.

Thus the results of the detailed mechanistic investigation carried out on the aqueous Barbier reaction strongly suggest the possibility of an allylzinc species as the reaction intermediate. This result is quite unexpected as the intermediacy of a radical anion formed through a single electron transfer from the metal surface was proposed earlier. This observation is also interesting from a synthetic point of view.

3. Dioxygen activation

A variety of metalloenzymes activate oxygen towards various biochemical oxidations, which would otherwise be forbidden due to the triplet state of oxygen. Considerable efforts have been made to understand the role of ligands in these systems to develop synthetic models that could perform the same under laboratory conditions.[5] The synthetic models developed so far suffer a serious limitation in that they are stable at very low temperatures and decompose at ambient temperature. There are instances wherein the peroxo species have been stabilized by steric hindrance or by hydrogen bonding.[6] However, details regarding the oxidizing ability of such stabilized species are unknown.

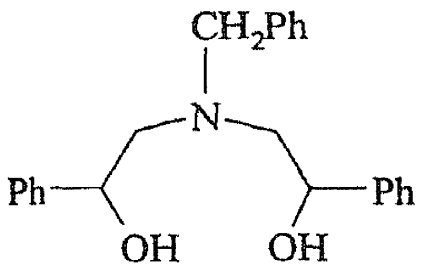

L2

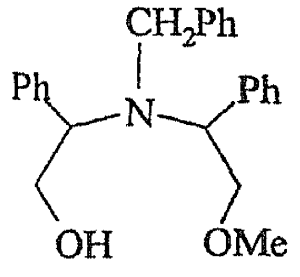

L2

Two ligands, **L1** and **L2**, containing nitrogen and oxygen donor sets have been used to synthesize copper(I) complexes that activate oxygen. The oxygenation of dichloromethane solutions of these complexes results in the formation of a green and a bluish green complex, respectively. In the presence of oxygen these complexes are in equilibrium with a complex containing a peroxo bridge. The peroxo bridge was detected by a chemical test for peroxide. They are reasonably stable at room temperature. Stability is attributed to hydrogen bonding by the ligand. However, attempts to crystallize these complexes failed. Instead, a colourless unstable copper(I) complex crystallized out from dichloromethane.

These complexes exhibit selective oxidation ability. The addition of two equivalents of PPh_3 to dichloromethane solutions of these complexes results in the formation of PPh_3O and the corresponding Cu(I)–PPh_3 complex. These complexes were also found to oxidize 3, 5-di-tert-butylcatechol catalytically to the corresponding quinone with a turnover number of 7.5. Similarly, benzylamine was found to be catalytically oxidized to the corresponding aldimine which after hydrolysis results in the formation of Schiff base adduct. This reactivity is different compared to the oxidation of amines to nitriles by $CuCl/O_2$/pyridine system.

The reactions observed with PPh_3 and 3,5-di-*tert*-butylcatechol suggest the presence of a μ–$\eta^2 : \eta^2$-peroxo moiety as the active species. However, the catalytic oxidation of catechol was found to be hampered by competing ligand oxidation, a limitation often encountered in catalytic oxidations. The product due to the ligand oxidation was obtained as a colourless liquid whose structure was not elucidated.

4. Metal–metal interactions

Short metal–metal distances are quite often observed in the solid-state structures of many di- and polynuclear metal clusters. It was earlier believed to result in metal–metal interactions in these systems. Metal–metal interactions in such systems depend largely on the coordinated ligands. They serve as a bridge through which the metals communicate. In many cases, the ligands force the metal centers to be in close proximity only to satisfy the bite angle requirements. *Ab initio* and Extended Huckel Theory (EHT) calculations serve as tools in understanding the nature of these metal–metal interactions.[7]

The role of bridging ligands (acetato, amidinato and triazenido) in mediating Pt–Pt interactions in dinuclear platinum(II) complexes were probed by EHT calculations. The computed reduced overlap population (ROP) suggests that M–M interactions are primarily affected by the electronic nature and relative disposition of the bridging ligands. Fragment molecular orbital analysis of these systems suggests that good π-acceptor ligands, triazenido for example, stabilize the metal–metal bond while the amidinato ligand destabilizes the metal–metal bond due to the lack of suitable π* orbitals.

References

1. Li, C. J. — *Chem. Rev.*, 1993, **93**, 2023.
2. Luche, J. L., Allavena, C., Petrier, C. and Dupuy, D. — *Tetrahedron Lett.*, 1998, **29**, 5373.
3. Zhang, H., Xue, F., Mak, T. C. W. and Chan, K. S. — *J. Org. Chem.*, 1996, **61**, 8002.
4. Einhorn, C. and Luche, J. L. — *J. Organomet. Chem.*, 1987, **322**, 177.
5. Kitajima, N. and Moro-oka, Y. — *Chem. Rev.*, 1994, **94**, 737.
6. El-Sayed, M. A., Ismail, K. Z. and El-Zayat, T. A. — *Inorg. Chim. Acta*, 1994, **217**, 109.
7. Aullon, G. and Alvarez, S. — *Inorg. Chem.*, 1996, **35**, 3137.